High Fidelity Ion Qubit State Detection

January 30, 2010

Abstract

This work demonstrates high-fidelity ion-qubit measurement, crucial not only for the read-out of states in the course of a computation, but also for effective quantum error correction. We trap and cool a single, or few, $^{88}Sr^{+}$ ions. A quantum bit is encoded in the two spin states of the single valence electron of the ion. Qubit readout is performed by shelving one of the qubit states to a metastable D level using a narrow linewidth laser at $674\,nm$ followed by state-selective fluorescence detection. To reach high fidelity qubit readout, the laser frequency has to be highly stabilized, and the linewidth of the laser has to be narrowed to the order of $1kHz$. For this purpose we use an external cavity diode laser at $674\,nm$ and lock it to an ultra low expansion glass reference cavity, thus reaching a relative frequency uncertainty of $\sim 10^{-12}$. Careful analysis of the statistics of the photons detected at the fluorescence stage, allows us to reach a detection error of $2 \cdot 10^{-3}$, compatible with recent estimates of the detection error threshold required for fault-tolerant computation.

Acknowledgments

First and foremost I would like to thank Dr. Roee Ozeri for introducing me to the world of experimental physics and showing me how exciting it is. Thank you for devoting so much time to give me both true insights to the nature of physics and valuable instruments for experimental work.

I would also like to thank Yinnon Glickman, together with whom I spent so many hours in the lab and to whom I owe the success of our mutual work. Thank you for your guidance and the invaluable knowledge you passed to me. Working with you has been a truly exciting experience (in so many senses of the word...).

To Shlomi Kotler, whose personal example set my way in experimental physics, go my special thanks. Your patience, combined with urge for clarity and accuracy helped me a lot along the way.

Nitzan Akerman - to your presence in the lab I owe my (partial) sanity. Your fresh ideas promoted the experiment greatly.

Last, but not least, Yehonatan Dallal, thank you for the help and encouragement along the way.

Contents

1 Introduction

A quantum computer performs computations using quantum mechanical principles for its operation. Several algorithms were introduced that make use of quantum mechanics to speed up different information processing tasks such as locating entries in a large database [4] or the efficient factorization of prime numbers [16].

Ideally quantum computers are more efficient than their classical counterparts for certain tasks. However, in the presence of noise quantum systems tend to "loose" their quantum nature or decohere. Moreover, the susceptibility of a quantum state to noise increases linearly with the dimension of the corresponding Hilbert space and therefore exponentially with the number of quantum bits (qubits). For this reason, quantum computers were considered as no more than a theoretical anecdote for a long time. Only in the last decade it was shown that by using active error-correction it is possible to actively suppress decoherence. Furthermore it was shown that if the error in any single quantum operation is smaller than a given, calculated, threshold a quantum register can involve an arbitrarily large number of qubits and still remain coherent to a large extent, thus mitigating the above exponential law.

Successful implementation of quantum algorithms, therefore, requires high fidelity state preparation, logic gates and state measurement. This work focuses on demonstration of high-fidelity ion-qubit measurement. It is important to note, that high accuracy state measurement is crucial not only for the readout of states in the computation, but is also a generic part of most quantum error correction protocols. The exact detection error threshold, required for fault tolerant quantum computation, depends on many factors such as the type of noise, the quantum error-correction protocol used and quantum register architecture, however under quite general assumptions error values of the orders of $10^{-2} - 10^{-4}$ were obtained [6].

In our experiment we trap and cool a single, or few, $^{88}Sr^{+}$ ions. A quantum bit is encoded in the two spin states of the single valence electron of the ion. The typical energy separation between the two Zeeman split spin states in the experiment is $\simeq 10\,MHz$. Qubit readout is done by shelving one of the qubit states to a metastable D level using a narrow linewidth laser at $674\,nm$ followed by state-selective fluorescence detection. To reach high fidelity in qubit readout, the laser frequency has to be highly stabilized, and the linewidth of the laser has to be narrowed to the order of $1\,kHz$. For this purpose we use an external cavity diode laser at $674\,nm$ and lock it to an ultra low expansion glass reference cavity. The relative frequency uncertainty of our shelving laser is $\sim 10^{-12}$. Finally, careful analysis of the statistics of the photons detected at the fluorescence stage, allows us to reach a detection error of $2 \cdot 10^{-3}$, compatible with recent estimates of the detection error threshold required for fault-tolerant computation.

2 Quantum bit

2.1 Two level system

A classical bit (binary digit) is a variable that can take one of two logical values - 0 or 1, that is be in one of the two physical states corresponding to these values. A qubit (quantum bit) is a quantum two state system. Meaning, it can be not only in one of the two states, but also in their arbitrary superposition. Usually the two states correspond to the two eigenstates of the unperturbed qubit. If we denote the two states by $|\downarrow\rangle$ and $|\uparrow\rangle$ - the most general superposition state, up to a global phase, can be written as

$$|\Psi\rangle = cos\left(\frac{\theta}{2}\right)|\downarrow\rangle + e^{i\varphi}sin\left(\frac{\theta}{2}\right)|\uparrow\rangle \tag{1}$$

and represented as a vector on a unit sphere (Bloch sphere representation) as shown in Fig. 1.

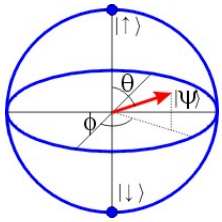

Figure 1: Bloch sphere representation of a two level system. The $|\uparrow\rangle$ and $|\downarrow\rangle$ states are represented by the north and south poles respectively. All states are characterized by the angles θ and ϕ indicating the direction of the Bloch vector.

2.2 Qubit measurement

One of the basic requirements for a physical implementation of a qubit, formulated by DiVincenzo [3], is the ability to faithfully measure it's state. If the qubit's state is given by the density matrix

$$\rho = p\,|\downarrow\rangle\langle\downarrow| + (1-p)\,|\uparrow\rangle\langle\uparrow| + \alpha\,|\downarrow\rangle\langle\uparrow| + \alpha^{\star}\,|\uparrow\rangle\langle\downarrow| \tag{2}$$

an ideal measurement should give outcome $|\downarrow\rangle$ with probability p and $|\uparrow\rangle$ with probability $(1-p)$, independent of α and of any other parameters of the system. A measurement can be also performed in a different basis. This is done by mapping the basis one would like to use for the measurement to the basis in which the actual measurement is performed. The mapping is done using qubit rotations. Note that the measurement discussed here is not a measurement of the exact state of the qubit. The exact state of a qubit can be found only given many copies of the qubit, e.g. using state tomography [?].

2.3 Fidelity and fault tolerance

Many quantum computation algorithms rely on long sequences of gating operations and qubit measurements. Suppose there is some error probability ϵ_0 in any single gate or measurement. The error in the result of a computation is $\epsilon \simeq 1-(1-\epsilon_0)^N$, where N is the total number of gates and measurements in the computation. The exponential dependence of the error on N prohibits large scale computation. However, we can use quantum error correction to protect states and decrease accumulated errors. It turns out that quantum computation with an arbitrary low error can be achieved even with noisy gates, using certain error correction schemes and provided that the single gate error is bellow a corresponding threshold [11]. In order to theoretically estimate the threshold for fault tolerant QIP the specific noise models assumed, quantum error-correction protocols used and the architecture of the quantum register, have to be taken into consideration. Recent estimates for fault tolerant error thresholds under assumptions that are quite general are of the orders of $10^{-2}-10^{-4}$.

The measurement error is defined as follows. For a qubit in state $\rho = |\downarrow\rangle\langle\downarrow|$ the probability for the outcome to be $|\downarrow\rangle$, in a perfect measurement, should be equal to 1. Due to imperfect measurement the probability is less than 1, namely $1-\epsilon_{|\downarrow\rangle}$. Similarly for a qubit in state $\rho = |\uparrow\rangle\langle\uparrow|$, the probability for the outcome to be $|\uparrow\rangle$ is in practice $1-\epsilon_{|\uparrow\rangle}$. The error of the measurement is the mean error $\epsilon = \frac{\epsilon_{|\uparrow\rangle}+\epsilon_{|\downarrow\rangle}}{2}$. The fidelity of the measurement is $F = 1-\epsilon$.

The experimental sequence used to find the measurement error consists of first initializing the qubit in the $|\downarrow\rangle$ state or the $|\uparrow\rangle$ state and then performing measurement. Therefore, the error due to imperfect state initialization will be added to the measurement error. The experiment is repeated many times for each of the qubit states, and the probabilities (fraction of experiments) $P(\downarrow|\uparrow)$, for the outcome of the measurement to be $|\downarrow\rangle$when the qubit is initialized in the $|\uparrow\rangle$ state, and $P(\uparrow|\downarrow)$, for the outcome of the measurement to be $|\uparrow\rangle$ when the qubit is initialized in the $|\downarrow\rangle$state, are obtained. Following the definition, the error is

$$\epsilon = \frac{P(\downarrow|\uparrow) + P(\uparrow|\downarrow)}{2}. \tag{3}$$

3 Physical implementation of quantum bits

3.1 Trapped $^{88}Sr^{+}$ ion

The physical implementation of a qubit in our system is based on the electronic energy states of an $^{88}Sr^{+}$ ion. To allow addressing of a single ion, it needs to be confined in a well defined and small region in space. Therefore it needs to be cooled and trapped.

3.1.1 Atomic level scheme and motional degrees of freedom

Strontium is an alkaline earth metal with two electrons in its valence shell. After a single ionization we get a Sr^{+} ion with only one valence electron, hence resembling an alkali atom. $^{88}Sr^{+}$ has no nuclear spin and accordingly no hyperfine structure. When a small magnetic field is applied ion's energy levels are Zeeman split. The relevant electronic energy levels and their Zeeman splittings are shown in Fig. 2.

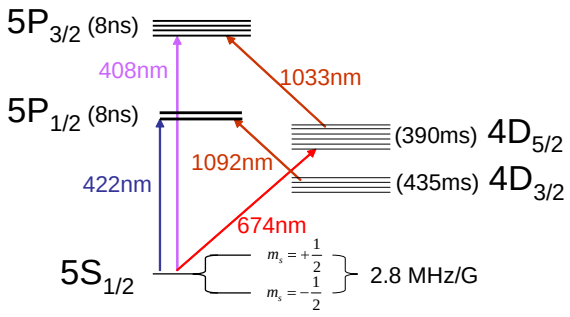

Figure 2: A schematic drawing of the relevant $^{88}Sr^{+}$ electronic energy levels

In addition to the internal energy levels of the ion, its motional degrees of freedom have to be taken into account. The ion is trapped in a pseudo-harmonic potential and hence can be treated as a 3D quantum harmonic oscillator. However, due to a strong confinement in two of the dimensions (the radial directions of the trap) , motional degrees of freedom along these directions can be usually neglected. The ion can then be treated as a 1D harmonic oscillator with energy levels given by $E_n = \hbar\omega_{trap}\left(n + \frac{1}{2}\right)$.

3.1.2 Optical qubit

To turn the ion into a qubit we need to choose two energy levels that will encode the $|\uparrow\rangle$ and $|\downarrow\rangle$ states. One option for this encoding is to use one of the states from the $S_{1/2}$ ground level as the

$|\downarrow\rangle$ state and one from the $D_{5/2}$ metastable ($390\,ms$) level as the $|\uparrow\rangle$ state. Such a qubit is called an optical qubit since the energetic separation between the two qubit levels is in the optical range ($4.45 \times 10^{14} Hz$, corresponding to a photon wavelength of $674\,nm$). The readout scheme for this qubit is relatively simple and will be explained in section 3.2.1. However, its lifetime is limited by the lifetime of the $D_{5/2}$ metastable level and is therefore relatively short. Moreover, both magnetic field and laser phase fluctuations lead to qubit dephasing.

3.1.3 Zeeman qubit

At zero magnetic field the $S_{1/2}$ ground level is doubly degenerate, due to the spin of the electron that can point in two opposite directions. When a magnetic field is applied, the two states are split as shown in Fig. 2. We can therefore encode the qubit in the Zeeman manifold of the $S_{1/2}$ ground level, choosing the $m_s = -\frac{1}{2}$ level to represent the $|\downarrow\rangle$ state and the $m_s = +\frac{1}{2}$ level to represent the $|\uparrow\rangle$ state. The splitting between the two energy levels is $2.8\frac{Mhz}{G}$. The natural lifetime of the $|\uparrow\rangle$ state is practically infinite. Here too, fluctuations in the ambient magnetic field will lead to qubit dephasing. However, contrary to optical qubit, the local oscillator for this qubit is in the RF range and therefore is not likely to limit qubit coherence due to phase fluctuations for a relatively long time.

3.2 Readout scheme

3.2.1 Optical qubit

For an optical qubit, state detection is performed using state-selective fluorescence. Detection is performed with a laser beam, resonant with the $S_{1/2} \rightarrow P_{1/2}$ transition. If the qubit is in the $|\downarrow\rangle$ state the ion will scatter photons in all directions (fluoresce) at a rate determined by the $P_{1/2}$ linewidth. We place a detector off of the $422\,nm$ laser beam axis and detect the scattered photons. However, if the qubit is in the $|\uparrow\rangle$ state laser light at $422\,nm$ cannot excite the ion and no scattered photons are observed.

3.2.2 Zeeman qubit

For a Zeeman qubit, in a small (few Gauss) magnetic field the above scheme can not be applied, since the energy splitting between the two qubit states is less than the spectral width of the $P_{1/2}$ level. Hence, both qubit states are simultaneously resonant and fluoresce. State detection of a Zeeman qubit is performed by first mapping the Zeeman qubit onto an optical one. This is done by shelving the electron from the $S_{1/2,+1/2}$ level (the $|\uparrow\rangle$ state) to one of the $D_{5/2}$ Zeeman split levels. Once the electron is shelved, state detection of an optical qubit is performed. The fidelity

of Zeeman qubit detection is therefore affected both by the electron shelving efficiency and optical qubit detection fidelity.

3.3 Laser-Ion interactions

3.3.1 Doppler cooling

Ion motion inside the trap decreases electron shelving efficiency, as is explained in section 3.3.4, and thus prevents high fidelity state detection of a Zeeman qubit. For this reason we want to decrease the thermal motion of the ion in the trap. This is equivalent to decreasing the mean harmonic oscillator level occupied by the ion, $\bar{n}$.

The first cooling stage we use is Doppler laser cooling on the $S_{1/2} \rightarrow P_{1/2}$ transition. Optimal cooling is achieved when the laser is detuned by half the excited level linewidth, $\frac{\Gamma}{2}$ red of the resonance. The temperature reached is

$$k_B T = \frac{\hbar\Gamma}{4}\left(1+\alpha\right), \tag{4}$$

where $\alpha = \frac{2}{5}$ the transition used for cooling is a dipole transition [**?**]. Assuming a Boltzmann distribution for the harmonic oscillator levels occupations

$$P_n = \frac{1}{\sum P_n} e^{-\frac{\hbar\omega_{trap} n}{k_B T}} = \frac{1}{\bar{n}+1}\left(\frac{\bar{n}}{\bar{n}+1}\right)^n, \tag{5}$$

where the mean occupation number satisfies

$$\bar{n} = \frac{1}{e^{\frac{\hbar\omega_{trap}}{k_B T}} - 1}. \tag{6}$$

Combining the last two equations we get

$$\bar{n} = \frac{1}{e^{\frac{4\omega_{trap}}{\Gamma(1+\alpha)}} - 1} \tag{7}$$

Substituting $\Gamma_{P_{1/2}} = 21\ MHz$ and $\omega_{trap} = 1.1\ MHz$ (the axial frequency of the trap), we obtain $\bar{n} \simeq 6.2$.

3.3.2 Optical pumping

As is discussed in section 2.3, part of the measured error is due to imperfect initialization of the qubit state. For a Zeeman qubit the initialization scheme is based on optical pumping using

circularly polarized light and is depicted in Fig. 3.

Photons are continuously scattered from a 422 nm laser beam resonant with the $S_{1/2} \rightarrow P_{1/2}$ transition. At a low magnetic field, Zeeman splitting between the two $S_{1/2}$ states is smaller than the width of the excited $P_{1/2}$ level ($\Gamma \simeq 21\, MHz$). Hence both spin states are excited. However, if the polarization of the 422 nm beam is σ^+, due to angular momentum conservation, only a $\Delta m_s = +1$ transition is allowed. Hence the $S_{1/2,-1/2}$ state is coupled to the $P_{1/2,+1/2}$ state, whereas the $S_{1/2,+1/2}$ state is does not couple to the $P_{1/2}$ level and is therefore dark. As the ion is excited to the $P_{1/2}$ level it spontaneously decays back to either of the two states - $S_{1/2,\pm 1/2}$. As this sequence is repeated, the $S_{1/2,-1/2}$ population decays exponentially with the number of photons scattered. This way all the population is eventually transferred to $S_{1/2,+1/2}$ and the qubit is initialized in the $|\uparrow\rangle$ state. Using a σ^- polarized beam the ion is initialized in the $|\downarrow\rangle$ state. The fidelity of this initialization procedure is limited by the polarization purity of the laser.

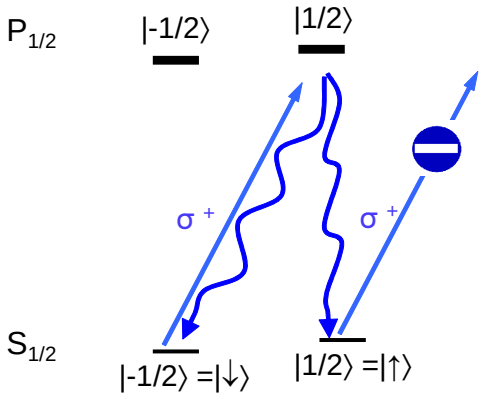

Figure 3: Schematic drawing of optical pumping. Straight lines represent laser beams, wiggly lines represent spontaneous decay.

3.3.3 Quadrupole transition

Electron shelving from the $S_{1/2,+1/2}$ state to the $D_{5/2}$ metastable level is done using narrow linewidth laser light at 674 nm. For a laser field given by $E = E_0 e^{i\left(\vec{k}\cdot\vec{r}-\omega t\right)} + c.c.$, where E_0 is the electric field amplitude, $\vec{k}$ is the wave-vector of the beam, $\vec{r}$ is the position operator and $\omega = ck$ is the light angular frequency. The position vector $\vec{r}$ can be decomposed to $\vec{r} = \vec{x} + \vec{r_e}$, where $\vec{x}$ is the location of the ion nucleus and $\vec{r_e}$ is the position of the electron relative to the nucleus. The $e^{i\vec{k}\cdot\vec{x}}$ part will then lead to a position dependent phase of the field, while the $e^{i\vec{k}\cdot\vec{r_e}}$ part can be treated using the standard long wavelength approximation. In first order (dipole) approximation, the $5S_{1/2} \rightarrow 4D_{5/2}$ transition is forbidden due to the equal parity of the S and the D levels. However, this transition is allowed in the next order (quadrupole) approximation. The

laser-ion interaction Hamiltonian can be written as

$$H_{int} = i\hbar\Omega_0 e^{i\left(\vec{k}\cdot\vec{x}-\omega t\right)}|n,S,m\rangle\langle n',D,m'| + h.c.\,, \tag{8}$$

where $n = 5$, $n' = 4$ are the principal quantum number of the corresponding energy levels. The Rabi frequency, Ω_0, denotes the coupling strength between the two levels and is given by [5]

$$\Omega_0 = \left|\frac{eE_0\omega_0}{2\hbar c}\langle n,S,m|\left(\vec{r}\cdot\vec{\epsilon}\right)\left(\vec{r}\cdot\vec{n}\right)|n',D,m'\rangle\right|. \tag{9}$$

Here $\vec{n}$ is a unit vector in the direction of $\vec{k}$ and $\vec{\epsilon}$ is the polarization of the field.
Note that Ω_0 depends on both the propagation direction and the polarization of the beam. For the beam configuration used in the experiment and shown in Fig. 8, the angle between the laser beam and the magnetic field $\phi\left(\vec{k},\vec{B}\right) = 0°$, hence the only allowed transitions are $\Delta m_J = \pm 1$ transitions, and the polarization of the beam does not change the Rabi frequency.

A detailed calculation of the Rabi frequencies for the relevant transitions is given in Appendix A.1. For a laser beam power of $120\,\mu W$ focused to a Gaussian waist of $\omega_0 = 30\,\mu m$ on the ion, the calculated Rabi frequencies are $\Omega_0\left(S_{1/2,1/2} \to D_{5/2,3/2}\right) = (2\pi)\,53\,kHz$ and $\Omega_0\left(S_{1/2,1/2} \to D_{5/2,-1/2}\right) = (2\pi)\,38\,kHz$.

3.3.4 Rabi flopping and the Lamb-Dicke regime

As was already mentioned in 3.1.1, the motion of the ion is mostly along the axial direction of the trap due to the strong confinement in the radial direction. This will be elaborated at the end of this section. For now, motional degrees of freedom along the radial direction will be neglected. The position vector $\vec{x}$ can be written as $\vec{x} = x\vec{e}_x$, where $\vec{e}_x$ is a unit vector along the axial direction of the trap. Recall that the position x of the ion is an operator and denote it by $\hat{x}$.

Using the harmonic oscillator raising and lowering operators $\hat{a}$ and $\hat{a}^\dagger$, the position operator of the ion $\hat{x}$ can be expended

$$\hat{x} = \sqrt{\frac{\hbar}{2m\omega_{trap}}}\left(\hat{a}+\hat{a}^\dagger\right)$$

and the interaction Hamiltonian becomes

$$\hat{H}_{int} = i\hbar\Omega_0 e^{i\left(\eta\left(\hat{a}+\hat{a}^\dagger\right)-\omega t\right)}|n,S,m\rangle\langle n',D,m'| + h.c.\,, \tag{10}$$

where

$$\eta = kcos\left(\phi\right)\sqrt{\frac{\hbar}{2m\omega_{trap}}} \tag{11}$$

is the Lamb-Dicke parameter. The angle between the axis of the trap ($\vec{e}_x$) and the direction of

laser light propagation ($\vec{n}$) is ϕ. In our experiment $\phi = 45°$ (see Fig. 8a), $\omega_{trap} = 1.1\ MHz$ and we calculate $\eta \simeq 0.12$. The interaction Hamiltonian can be expended in orders of η

$$e^{i\eta\left(\hat{a}+\hat{a}^\dagger\right)} = 1 + i\eta\left(\hat{a}+\hat{a}^\dagger\right) - \frac{\eta^2\left(\hat{a}+\hat{a}^\dagger\right)^2}{2} + ... \tag{12}$$

To 0^{th} order in the expansion, the interaction Hamiltonian is simply

$$\hat{H}_{int} = i\hbar\Omega_0 e^{-i\omega t}|n,S,m\rangle\langle n',D,m'| + h.c.$$

In the interaction picture representation (or equivalently, in a rotating wave frame with respect to the ion) it is transformed to

$$\hat{H}_{int} = i\hbar\Omega_0 e^{-i\Delta t}|S,m\rangle\langle D,m'| + h.c.\,,$$

where $\Delta = \omega - \omega_0$ is the detuning of the laser frequency from the resonant transition frequency ω_0. Assuming Δ is large with respect to Ω_0 for all $S_{1/2,m} \rightarrow D_{5/2,m'}$ transitions except for one, and performing the rotating wave approximation we end up with a two level system described by standard Rabi oscillations. For the initial conditions $P_\downarrow(t=0) = 1$, time dependent population inversion is given by $P_\uparrow(t) = P_{\uparrow,max} sin^2\left(\frac{\Omega_R t}{2}\right)$. The oscillation frequency is $\Omega_R = \sqrt{\Omega_0^2 + \Delta^2}$ and the maximal population inversion is $P_{\uparrow,max} = \frac{\Omega_0^2}{\Omega_0^2+\Delta^2}$. Notice that in this case no HO creation or annihilation operators appear in $\hat{H}$ and therefore the motion of the ion as unaffected by light. This excitation preserves the HO level n and is referred to as the carrier excitation.
Including higher orders of η, the first term in the expansion allows transitions from the n^{th} motional state to the $n \pm 1^{th}$ states. The effective coupling strength for these sideband transitions are

$$\Omega_{n,n+1} = \Omega_0\langle n+1|i\eta\left(\hat{a}+\hat{a}^\dagger\right)|n\rangle = i\Omega_0\eta\sqrt{n+1} \tag{13a}$$

and

$$\Omega_{n,n-1} = \Omega_0\langle n-1|i\eta\left(\hat{a}+\hat{a}^\dagger\right)|n\rangle = i\Omega_0\eta\sqrt{n}\,. \tag{13b}$$

The $n \rightarrow n+1$ $(n-1)$ transition is referred to as the Blue (Red) sideband transition.
The next term (second order in η) allows transitions from the n^{th} motional state to the $n \pm 2^{th}$ state and also gives a small correction to the carrier transition Rabi frequency $\Omega_{n,n} = \Omega_0\left(1 - \eta^2\left(n + \frac{1}{2}\right)\right)$. Although small, this correction limits electron shelving efficiency at a finite temperature as is shown bellow.
Assume the ion has some harmonic oscillator levels occupation distribution. Initially in the $|\downarrow\rangle$ state and with an ideal laser, resonant with the carrier transition, the probability of finding the

ion in the $|\uparrow\rangle$ state as function of time is

$$P_{\uparrow}(t) = \Sigma p_n P_{\uparrow,n}(t) = \Sigma p_n P_{\uparrow,n,max} sin^2\left(\frac{\Omega_{R,n} t}{2}\right) , \tag{14}$$

where p_n is the probability of the ion being in the n^{th} harmonic oscillator level. For p_n following a thermal distribution with $\bar{n} \simeq 6.2$, the lowest value reachable with Doppler cooling in our trap, the time evolution for $P_{\uparrow}(t)$, at zero detuning, is plotted in Fig. 4. As seen, dephasing between the different Rabi frequencies, corresponding to different n, limit the maximal population inversion reached to $P_{\uparrow,max} \simeq 0.97$.

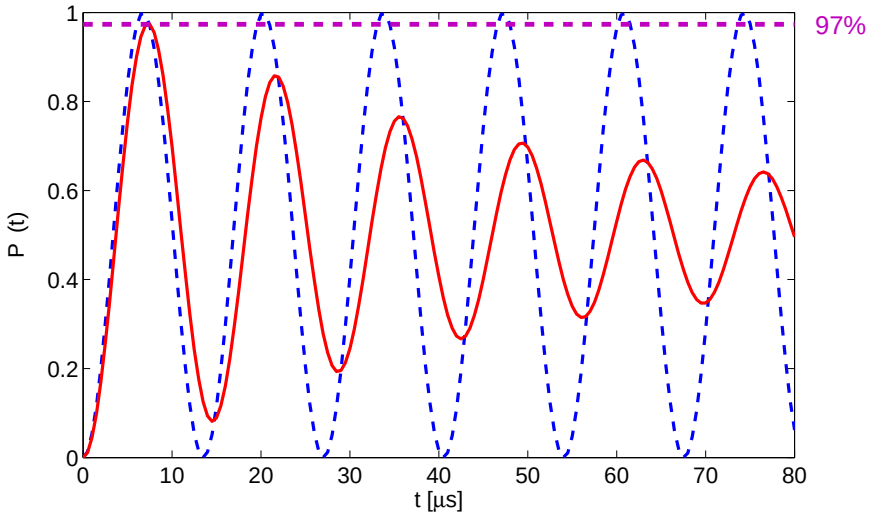

Figure 4: Population inversion as function of time for detuning $\Delta = 0$. The blue dashed line shows Rabi oscillations for an ion in the ground state of the HO ($T = 0$). The red solid line shows Rabi oscillations for a thermal distribution in the occupation of HO levels, with $\bar{n} \simeq 6.2$ ($T \simeq 55\,\mu K$).

Now consider the affect of the radial motion of the ion. Since the 674 nm laser $\vec{k}$ vector has a component in the radial direction of the trap as well (see Fig. 8a), the Lamb-Dicke parameter for the radial motion will be non zero and the distribution of radial harmonic level numbers will also have an affect on the shelving efficiency. However, due to the stronger confinement in the radial direction $\omega_r > \omega_{ax}$ the effect is much smaller. The angle between the radial direction of the trap and the direction of laser light propagation is $\phi = 45°$. The radial trap frequency is $\omega_r \simeq 2.5 MHz$. According to Eqs. 7 and 11 the mean harmonic level occupation number is $\bar{n_r} \simeq 2.5$ and the Lamb-Dicke parameter is $\eta_r \simeq 0.08$, leading to an estimated population inversion error of $\simeq 0.2\%$. This compares to the previously calculated $\simeq 3\%$ error due to the axial motion.

4 State discrimination

As was mentioned in 3.2, qubit state detection is based on the statistics of photons detected by the PMT. However, a well defined criterion for state discrimination is required. In order to find the optimal criterion and to estimate its fidelity, the statistics of photon detection events are analyzed in detail. In this section two different methods of state discrimination are presented, and the effect of imperfect state preparation and shelving are discussed.

4.1 Cutoff method

4.1.1 Perfect state preparation

The number of photons n, detected by the PMT during a given detection time t_{det} is a random variable. This random variable will be denoted by n_b if the ion is in the fluorescing (bright) state $S_{1/2}$, and n_d if the ion is in the non-fluorescing (dark) state $D_{5/2}$. Photons are detected when the ion is in the dark state due to detectors dark counts, background room light and scattering and mainly due to scattering of the laser beam from trap surfaces. The efficiency of state discrimination is determined by the overlap of the probability distribution functions (PDFs) of these two random variables.

The simplest way to discriminate between the two states is to introduce a cutoff on the number of photons detected, n_c. If the number of photons detected is greater than this cutoff, $n > n_c$, then we infer that the ion is in the bright state. Whereas, if the number is smaller, $n \leqslant n_c$, we infer that the ion is in the dark state. Given the probability distribution functions for n_b, n_d we find the error in the detection of the bright and dark states to be $\epsilon_b = p_b\left(n \leqslant n_c\right)$ and $\epsilon_d = p_d\left(n > n_c\right)$ respectively. We want to find the parameters t_{det}, n_c that minimize the mean error

$$\epsilon = \frac{\epsilon_b + \epsilon_d}{2} = \frac{p_b\left(n \leqslant n_c\right) + p_d\left(n > n_c\right)}{2}. \tag{15}$$

To find the PDFs, first assume that the lifetime of the $D_{5/2}$ level is infinite. Hence, the ion does not decay to the fluorescing $S_{1/2}$ state during the detection period. In this case the random variables n_b, n_d follow a Poisson distribution. The mean of these distributions $\bar{n}_b$ and $\bar{n}_d$ increase linearly with detection time, t_{det}. More specifically, given photon detection rates R_b and R_d in the bright and dark state respectively, the means are $\bar{n}_{b,d} = R_{b,d} t_{det}$. The two distribution functions are plotted in Fig. 5a. Clearly, as the detection time is increased the overlap between the two PDFs decreases, resulting in higher state discrimination fidelity.

Now consider the affect of the $D_{5/2}$ level finite lifetime. Assume that the ion is initially in the $D_{5/2}$ state. As long as it remains in this dark state, the photon detection rate is R_d. For a

given time $t^\star$, the probability the ion decays to the $S_{1/2}$ ground state level at $t < t^\star$ is given by $P(t^\star) = 1 - e^{-t^\star/\tau}$, where τ is the lifetime of the $D_{5/2}$ level. Upon decay, the photon detection rate becomes R_b. Therefore, the probability to detect n photons during the time t_{det} is

$$p_d(n) = \left(1 - \frac{t_{det}}{\tau}\right) Poiss(n,\, R_d t_{det}) + \int_0^{t_{det}} dt' \frac{1}{\tau} \sum_{k=0}^{n} Poiss(k,\, R_d t')\, Poiss(n-k,\, R_b(t_{det} - t'))\,. \quad (16)$$

Here $Poiss(n,\, \bar{n})$ denotes the probability to detect n photons for a Poissonian distribution with mean $\bar{n}$. The first term in Eq. 33 accounts for the case in which the ion did not decay. The second term integrates over the periods of time dt' at which decay occurred. The probability for decay to happen during the time period $(t',\, t' + dt')$ is $\frac{dt'}{\tau} e^{-t'/\tau}$ and can be approximated by $\frac{dt'}{\tau}$ for $t' < t_{det} \ll \tau$. For any $0 < t' < t_{det}$, the total number of photons detected is both due to photons scattered while the ion was in the dark state during the time period $(0,\, t')$, and due to photons scattered when the ion was in the bright state during the time period $(t',\, t_{det})$. Hence the sum over all possible combinations of photons scattered during the two periods appears. This sum can be simplified to give

$$\sum_{k=0}^{n} Poiss(k,\, R_d t')\, Poiss(n-k,\, R_b(t_{det} - t')) = Poiss(n,\, \bar{n})\,. \quad (17)$$

Hence, if the decay occurred at some instance $0 < t' < t_{det}$, the number of detected photons still follows a Poissonian distribution, with the weighed mean $\bar{n} = \bar{n}_d \frac{t'}{t_{det}} + \bar{n}_b \left(1 - \frac{t'}{t_{det}}\right)$. Equation 33 can then be written explicitly

$$p_d(n) = \left(1 - \frac{t_{det}}{\tau}\right) Poiss(n,\, \bar{n}_d) + \frac{t_{det}}{\tau} \frac{\Gamma(\bar{n}_b\, n + 1) - \Gamma(\bar{n}_d,\, n+1)}{\bar{n}_b - \bar{n}_d} \quad (18)$$

using the incomplete gamma function $\Gamma(x, a) = \frac{1}{\Gamma(a)} \int_0^x e^{-t} t^{a-1} dt$. See Appendix A.2 for a detailed derivation of Eqs. 17 and 18. The obtained PDF for n_d is shown in Fig. 5b together with the PDF for n_b which is unaffected by the finite lifetime of the $D_{5/2}$ level, for $t_{det} = 10^{-3}\tau$. Note the increase in the overlap between the two functions.

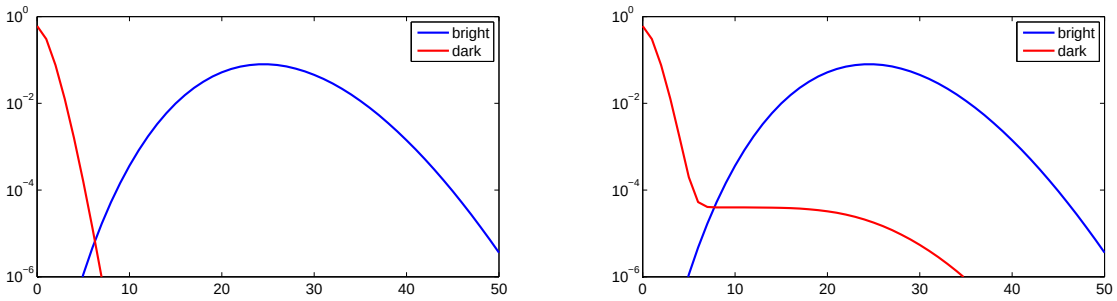

(a) (b)

Figure 5: Probability density functions for the number of photons detected by the PMT in the dark ($D_{5/2}$, red) and the bright ($S_{1/2}$, blue) states. (a) Assuming infinite dark state lifetime. (b) A finite lifetime $\tau = 10^3 t_{det}$ of the $D_{5/2}$ level is taken into account.

Here, as the detection time is increased the overlap between the two functions initially drops, due to the larger spacing between the two Poisson peaks, but at some point starts increasing due to the growing tail of the dark distribution. Hence an optimal detection time and threshold number of photons exist such that the efficiency of state discrimination is maximal. Figure 6 shows a contour plot for the state discrimination error, defined in Eq. 15, as function of the detection time t_{det} and the cutoff on the number of photons n_c. Our measured detection rates of $R_b = 65\,kHz$, $R_d = 1.3\,kHz$ are used, as well as the known lifetime of the $D_{5/2}$ level, $\tau_{D_{5/2}} = 390\,ms$ [8].

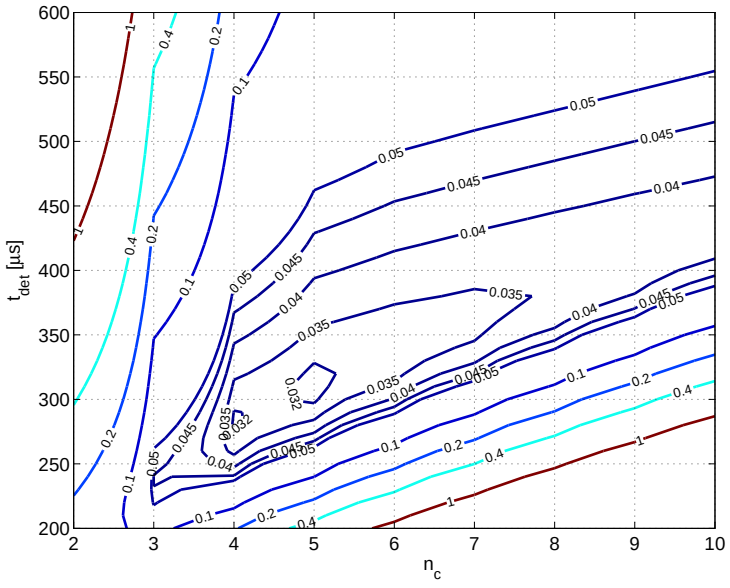

Figure 6: Contour plot of the state discrimination error (in %) as function of the detection time t_{det} and the cutoff on the number of photons n_c. Measured detection rates for the system $R_b = 65kHz$, $R_d = 1.3kHz$ are used, as well as the known lifetime of the $D_{5/2}$ level, $\tau_{D_{5/2}} = 390ms$.

A minimal error of $\epsilon \simeq 3 \cdot 10^{-4}$ is calculated at a detection time of $t_{det} = 310\mu s$ and a cutoff on the number of photons of $n_c = 5$.

4.1.2 Imperfect state initialization

The actual distributions measured in the experiment are also affected by state preparation error, and an error resulting from an imperfect shelving of the ion to the metastable state. The state preparation errors, $\epsilon_{b,init}$ and $\epsilon_{d,init}$ for the bright and dark states respectively, are the fraction of experiments in which the ion was initialized in the wrong state. The shelving error for the dark state $\epsilon_{d,shelving}$ is the probability that the ion remained in the $S_{1/2}$ level after shelving was performed. For the bright state, $\epsilon_{b,shelving}$ is the probability that the ion was shelved to the $D_{5/2}$ level due to off-resonant light. The resulting PDFs for the bright and dark states are given by

$$\tilde{p}_b(n) = (1-\epsilon_{b,init})(1-\epsilon_{b,shelving})\,p_b(n) + [\epsilon_{b,init}(1-\epsilon_{d,shelving}) + (1-\epsilon_{b,init})\,\epsilon_{b,shelving}]\,p_d(n) \quad (19a)$$

and

$$\tilde{p}_d(n) = (1-\epsilon_{d,init})(1-\epsilon_{d,shelving})\,p_d(n) + [\epsilon_{d,init}(1-\epsilon_{b,shelving}) + (1-\epsilon_{d,init})\,\epsilon_{d,shelving}]\,p_b(n) \quad (19b)$$

respectively. Here $p_d(n)$ is the dark distribution given by Eq. 18.

Since all errors $\epsilon_{b/d,init/shelving}$ and $\frac{t_{det}}{\tau}$ are small (of the order of 10^{-3}), second order errors can be neglected and we get,

$$\tilde{p}_b(n) \simeq (1-\epsilon_{b,tot})\,Poiss(n,\bar{n}_b) + \epsilon_{b,tot}Poiss(n,\bar{n}_d) \quad (20a)$$

$$\tilde{p}_d(n) \simeq \left(1-\epsilon_{d,tot}-\frac{t_{det}}{\tau}\right)Poiss(n,\,\bar{n}_d) + \frac{t_{det}}{\tau}\frac{\Gamma(\bar{n}_b\,n+1)-\Gamma(\bar{n}_d,\,n+1)}{\bar{n}_b-\bar{n}_d} + \epsilon_{d,tot}Poiss(n,\bar{n}_b) \quad (20b)$$

Note that only the sum of the initialization error and the shelving error appears $\epsilon_{b/d,tot} = \epsilon_{b/d,init} + \epsilon_{b/d,shelving}$. This prevents us from distinguishing state preparation error from state detection error.

The total mean detection error,

$$\tilde{\epsilon} = \frac{\tilde{\epsilon}_b + \tilde{\epsilon}_d}{2} = \frac{\tilde{p}_b\left(n \leqslant n_c\right) + \tilde{p}_d\left(n > n_c\right)}{2}, \tag{21}$$

can be related to the error ϵ resulting from the finite lifetime of the metastable level alone, obtained in section 4.1.1

$$\tilde{\epsilon} = \epsilon\left(1 - \left(\epsilon_{b,tot} + \epsilon_{d,tot}\right)\right) + \frac{\epsilon_{b,tot} + \epsilon_{d,tot}}{2} \simeq \epsilon + \frac{\epsilon_{b,tot} + \epsilon_{d,tot}}{2}. \tag{22}$$

In particular, the minimum of $\tilde{\epsilon}$ is obtained for the same values of detection time t_{det} and cutoff on the number of photons n_c, as the minimum of ϵ.

4.2 Photon arrival times

For better state discrimination, the state-dependent likelihood of detecting not only a certain number of photons also their arrival times sequence can be considered.. Using this information some of the events in which the ion decayed during the detection time and scattered more than n_c photons can be identified. Therefore, using this method ϵ_d can be decreased. Given a set of photon arrival times $\{t_i\}$ we calculate the likelihood for this set to be obtained given that the ion was in the bright state p_b, and similarly for the dark state p_d. If $p_b > p_d$ we conclude the ion was in the bright state, and vice verse.

For convenience, each data set is arranged in bins of duration $t_{bin} = 10\mu s$ and the number of photons in each bin $\{n_i\}$ is considered. The number of bins is $N = \frac{t_{det}}{t_{bin}}$. Then, using a similar treatment to Myerson *et al.* [10] the corresponding PDFs are

$$p_b\left(\{n_i\}\right) = \prod_{i=1}^{N} Poiss\left(n_i,\ R_b t_{bin}\right) \tag{23a}$$

$$p_d\left(\{n_i\}\right) = \left(1 - \frac{t_{det}}{\tau}\right)\prod_{i=1}^{N} Poiss\left(n_i,\ R_d t_{bin}\right) + \frac{t_{bin}}{\tau}\sum_{j=1}^{N}\prod_{i=1}^{j-1} Poiss\left(n_i,\ R_d t_{bin}\right)\prod_{i=j}^{N} Poiss\left(n_i,\ R_b t_{bin}\right) \tag{23b}$$

The improvement in detection efficiency is primarily due to dark events in which the decay occurred late enough, such that the time distribution of photon detection times is highly non-uniform. These events will now be correctly identified as dark. Assuming that these events correspond to decay times $t_{decay} \geqslant \frac{1}{2}t_{det}$, we get a rough estimate on the decrease of the dark error from ϵ_d to $\frac{1}{2}\epsilon_d$. Since the bright error is unaffected by this process the total error reduces from ϵ to $\frac{3}{4}\epsilon$. Using the value of $\epsilon \simeq 3 \cdot 10^{-4}$ obtained in section 4.1.1, this corresponds to a small error reduction of $\sim 10^{-4}$.

5 Ion trap apparatus and lasers

5.1 RF Paul trap

The ions are trapped in a linear RF Paul Trap [12]. A generic configuration of such a trap is shown in Fig. 7.

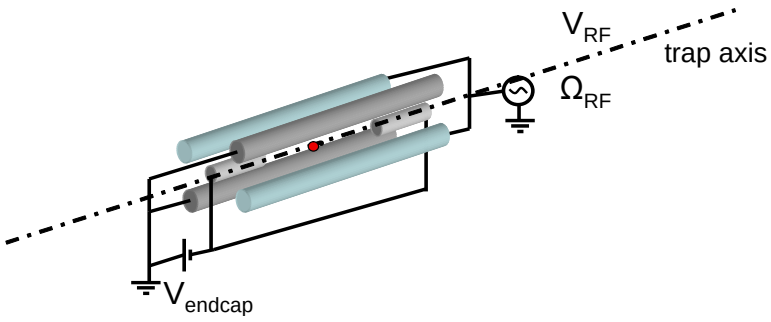

Figure 7: A schematic drawing of a linear RF Paul trap. The ion in the middle of the trap is indicated in red. Two short electrodes on both sides of the ion are held at a constant voltage V_{DC}. The Light blue electrodes are connected to an RF source oscillating at frequency Ω_{RF} and amplitude V_{RF}, and the remaining two electrodes are grounded.

The ion is captured in the trapping region between the end-cap electrodes held at a DC voltage of $V_{endcaps} \simeq 5 - 60\,V$. Two other electrodes are connected to an RF source oscillating at frequency $\Omega_{RF} \simeq 20\,MHz$ and with an amplitude $V_{RF} \simeq 100 - 200\,V$. The last two electrodes are grounded. The potential formed by this configuration is approximately an electric quadrupole potential. The end-caps constantly confine the positively charged ion in the axial direction (along the trap axis). In the radial direction - during one half of the oscillation period the ion is confined in one axis and anti-confined in the other, whereas during the second half of the period the directions of confinement and anti-confinement are interchanged. Due to these rapid oscillations the ion doesn't have enough time to escape from the trap and rather its motion is dominantly governed by a resulting pseudo pondermotive potential. A full treatment of the motion of the ion in RF Paul traps, both classical and quantum, is given in references [7, 19]. The pseudo-potential can be well approximated to be harmonic in all three directions. The effective harmonic oscillator frequencies in the radial direction ω_r and in the axial direction ω_{ax} depend both on V_{RF} and on $V_{endcaps}$. In our experiment the radial (axial) trap frequency is $\omega_r \simeq 2.5MHz$ ($\omega_{ax} \simeq 1.1MHz$).

5.2 RF electrode

Direct coupling between the two Zeeman states of the $S_{1/2}$ ground level is achieved via magnetic dipole coupling, $H_{int} = -g\vec{B} \cdot \vec{S}$. Resonant coupling occurs when a small magnetic field, perpendicular to the quantization field oscillates at a frequency matching the Zeeman separation between

the states. To this end, we drive an oscillating current through an additional electrode which is parallel to the trap axis. The ion electrode distance is $1.7\,mm$. An arbitrary waveform generator (Keithley model 3390) is used to push a current of $I = 200\,mA$, impedance matched to $1\,\Omega$. The current is a sine wave oscillating at Zeeman splitting frequency of $\omega_{Zeeman} \simeq (2\pi)\,10.7MHz$. The resulting Rabi oscillation observed on the $S_{1/2,1/2} \rightarrow S_{1/2,-1/2}$ transition has a period of $16\,\mu s$ ($t_\pi \simeq 8\mu s$).

5.3 Magnetic field

To remove the degeneracy between the different Zeeman levels and to have a well defined quantization axis we need a controlled stable magnetic field on the trapped ion. The control of the magnetic field on the ion is achieved via three orthogonal Helmholtz pairs of coils located around the trap vacuum chamber as shown in Fig. 8b. Two sets of coils - horizontal and vertical - are used to cancel any stray (e.g. earth) magnetic DC field orthogonal to the quantization axis. The third pair (quantization coils) are used to set the desired energy level splitting and define the quantization axis direction. We typically work at a current of $\simeq 250\,mA$ through the coils providing a magnetic field of $\simeq 4\,G$ on the ion.

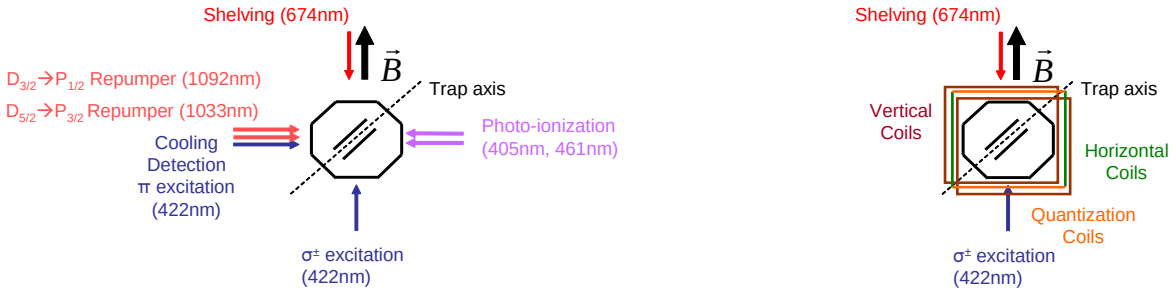

(a) (b)

Figure 8: Vacuum chamber, laser beams and magnetic field coils layout. (a) The propagation direction of the $674\,nm$ laser forms an angle $\phi = 45°$ both with the axial and the radial direction of the trap. (b) The quantization coils are used to generate magnetic field along the designated direction. The vertical and horizontal coils are used to cancel any stray magnetic DC field in the orthogonal directions.

5.4 Imaging system

As was discussed in section 3.2 the detection of qubit state is eventually based on the detection of spontaneously scattered photons. The direction of fluorescence collection is perpendicular to the quantization axis and the laser beams propagation plane. A 0.31 numerical aperture objective lens that corrects for the view-port spherical aberrations collects fluorescence light from the ion. A

flipping mirror switches between two possible measurements: either a diffraction limited imaging of the ions onto a CCD camera, or single photon counting by two photomultiplier tubes (PMT) each on a different side of a polarizing beam splitter (PBS) cube.

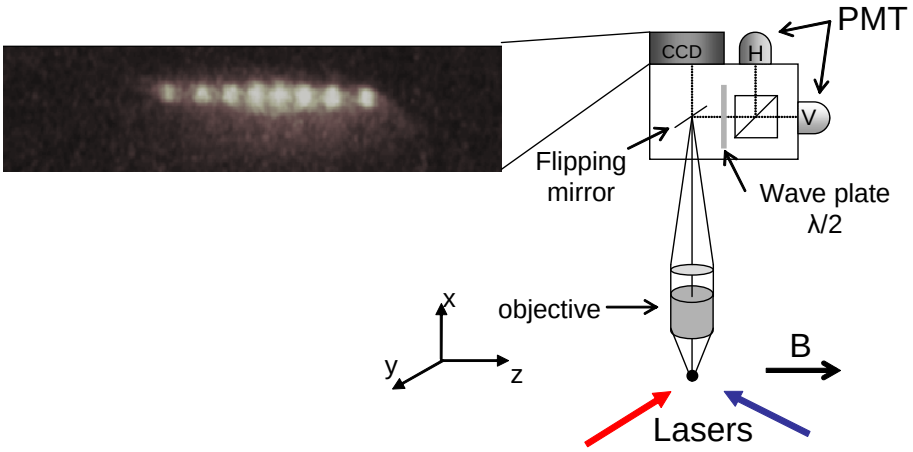

Figure 9: Schematic drawing of the imaging system. A 0.31 numerical aperture objective lens collects fluorescence light from the ion. A flipping mirror is used to switch between diffraction limited imaging of the ions onto a CCD camera and single photons counting by two photomultiplier tubes (PMT) each on a different side of a polarizing beam splitter (PBS) cube.

5.5 Loading of the trap

The trap is loaded by photo-ionizing neutral Strontium atoms from a thermal beam intersecting the trap center. A thermal beam of Sr atoms is produced by resistively heating a cannon-shaped Sr oven pointing towards the center of the trap. The ionization of the neutral Sr is performed by two-photon ionization. First a 461 nm laser, generated by a 921 nm diode laser doubled in a periodically poled KTP (PPKTP) non-linear crystal, transfers the ion to $5s5p\,{}^1P_1$ level. The spectral width of this level is $(2\pi)\,32\ MHz$. The laser beam is roughly perpendicular to the Sr beam to avoid Doppler broadening. Then a free-running 405 nm diode laser transfers it to the auto-ionizing level $5p^2\,{}^1D_2$. The spectral width of this auto-ionizing state is 1 nm.

5.6 Doppler cooling, optical pumping and fluorescence detection - 422 nm

Doppler cooling, optical pumping and detection are all done with a laser close to resonance with the $S_{1/2} \rightarrow P_{1/2}$ transition at 422 nm. The 422 nm laser is a doubled diode laser manufactured by Toptica. The fundamental light is generated by a 844 nm laser and is frequency doubled using am intra-cavity non-linear crystal. The cavity is locked to the laser by the method of Pound-Drever-Hall, leading to a relatively high doubling efficiency (10%). The emission wavelength is locked to a ${}^{87}Rb$ line at 422 nm, which is only 440 MHz red of the $S_{1/2} \rightarrow P_{1/2}$ transition of ${}^{88}Sr^+$.

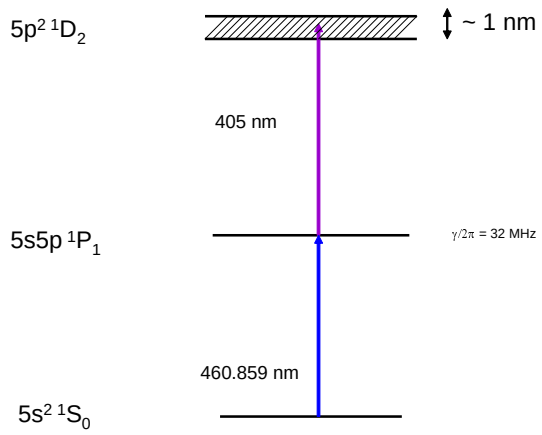

Figure 10: Two-photon ionization scheme for Sr.

5.7 $D_{3/2}$ repumping - $1092\,nm$

Spontaneous decay from the $P_{1/2}$ level has a $\simeq \frac{1}{14}$ probability to be to the $D_{3/2}$ metastable state. The $1/e$ lifetime of this level is $\tau_{D_{3/2}} \simeq 440ms$ and therefore, unless repumped, during this, relatively long, period of time no operations on the ion can be carried out. To repump the ion from the $D_{3/2}$ level back to $P_{1/2}$ level we use a DFB diode laser at $1092\,nm$ (Toptica, model DL100 DFB) . The laser is locked to a home built, sealed, Invar cavity using the Hänsch-Couillaud method for intermediate term stability. For longer term stability the Invar cavity is locked in turn to an, in vacuum, Zerodur cavity via the $1033\,nm$ light (see below).

5.8 Electron shelving - $674\,nm$

Zeeman qubit state detection is done by shelving the electron in the $S_{1/2,1/2}$ state to the $D_{5/2}$ metastable state, using a narrow linewidth diode laser at $674\,nm$. A detailed description of this laser is given in section 6.

5.9 $D_{5/2}$ repumping - $1033nm$

Once the electron is shelved to the $D_{5/2}$ state it remains there for a mean time of $\tau_{D_{5/2}} \simeq 390ms$ ($D_{5/2}$ metastable state $1/e$ lifetime) before it decays back to the ground state. For high repetition rate of the experiment the electron has to be repumped out of the $D_{5/2}$ state via the $P_{3/2}$ state, which has a $1/e$ lifetime of $\tau_{P_{3/2}} \simeq 8\,ns$. This is done using a diode laser at $1033\,nm$ (Toptica, model DL100). The laser is locked to an in vacuum Zerodur cavity (thermal expansion coefficient $\alpha \simeq 10^{-7}\frac{1}{K}$), using the lock-in method, for long term frequency stability. Note that once the electron is repumped to the $P_{3/2}$ state, it has a small, though finite probability, to decay to the $D_{3/2}$ state. Therefore the $1092\,nm$ laser has to be on during the repumping.

6 Narrow linewidth diode laser at $674\,nm$

High fidelity Zeeman qubit readout requires the $674\,nm$ laser used for shelving to have a spectral linewidth much narrower than its Rabi frequency. As mentioned in section 3.3.3 the expected Rabi frequency is of the order of $50\,kHz$. Thus for high fidelity Zeeman qubit detection the linewidth of the laser has to be on the order of $1\,kHz$. A typical linewidth of a laser diode however is of the order of a few tens of MHz. In addition, a long term frequency stability (on the order of few kHz) is required to keep the laser on resonance with the $S_{1/2} \rightarrow D_{5/2}$ transition. Both requirements are fulfilled by using an external cavity for the diode laser and locking the laser to a high finesse ultra-stable cavity as described bellow.

6.1 $674\,nm$ laser scheme

The basic scheme for the $674\,nm$ laser is shown in Fig. 11. An acousto-optic deflector (AOD) in a double-pass configuration is used to shift the frequency of the laser before it's locked to an in-vacuum ($10^{-8}\,Torr$) high finesse Ultra Low Expansion (ULE) Glass cavity using a PDH locking method. This method requires phase modulation at a high frequency which is done by an EOM. The error signal used for feedback on the laser is extracted from demodulation of the signal reflected from the cavity. Before hitting the ion, the laser beam frequency is shifted with an Acousto-Optic Modulator (AOM) switch.

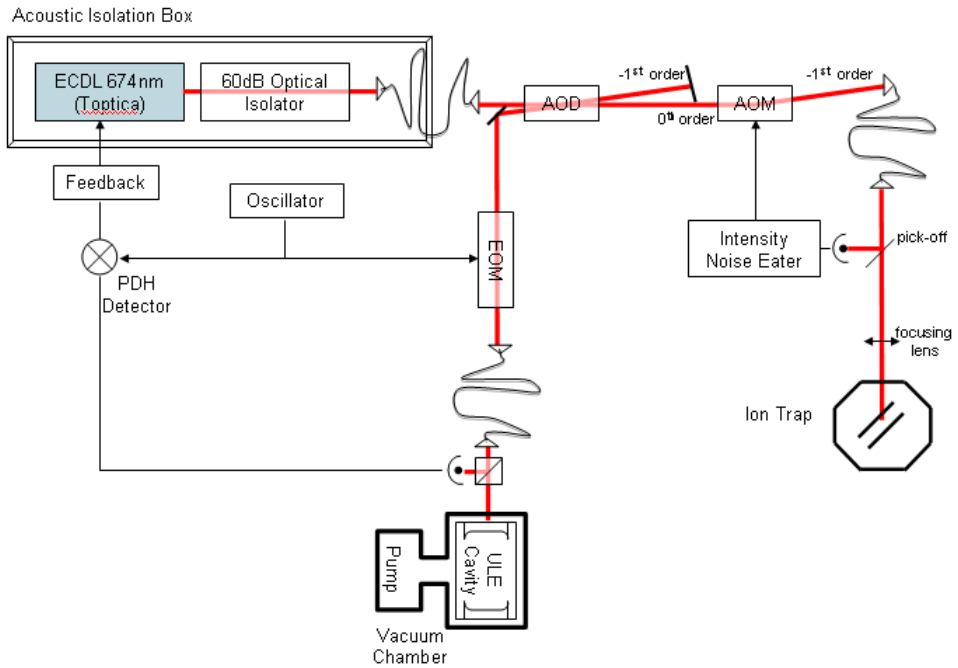

Figure 11: Schematic drawing of the $674\,nm$ laser frequency and intensity feedback loops. Red lines represent the propagation of laser light.

The AOM frequency is computer controlled. The AOM allows for fast ($< 1\,\mu s$) on-off switching of beam. The switch AOM also controls the laser intensity by varying its input RF. We then use this control to stabilize the laser intensity to a fixed value via a closed loop as described in Sec. 6.4. The different frequencies appearing in this scheme and relations between them are shown in Fig. 12.

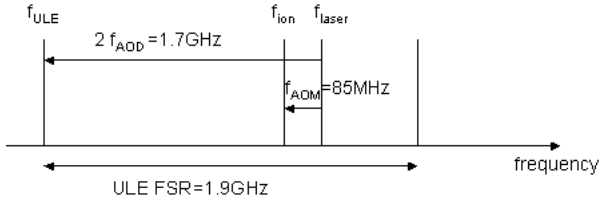

Figure 12: Schematic drawing of the 674 nm laser frequencies. The AOD shifts the frequency of the laser to a frequency coinciding with a resonant line of the ULE cavity. The AOM compensates for the frequency difference between the laser and the resonance of the ion.

6.2 Frequency stabilization and linewidth narrowing

6.2.1 Laser linewidth and diode laser frequency noise

A noisy laser field can be written in the form

$$E(t) = E_0(1 + \epsilon(t))e^{i(\omega_0 t + \phi(t))}, \tag{24}$$

where $\epsilon(t)$ corresponds to amplitude noise, and $\phi(t)$ corresponds to phase noise. Since amplitude noise is relatively small in diode lasers above lasing threshold we neglect it hereafter. Phase noise is related to frequency noise by $2\pi\delta\nu(t) = \omega_{inst}(t) - \omega_0 = \dot{\phi}(t)$.

The optical spectrum is defined by $I(\omega) = \left|\tilde{E}(\omega)\right|^2$ where $\tilde{E}(\omega)$ is the Fourier transform of the laser field, $E(t)$. The linewidth of a laser is the Full Width at Half Maximum (FWHM) of its optical spectrum. The lineshape and linewidth of a laser depend on the type of frequency noise present. Different types of noise are usually characterized by their Power Spectral Density (PSD). The PSD, $S_{\delta\nu}(\omega)$, of a given frequency noise is the Fourier transform of the noise auto-correlation function, $R_{\delta\nu}(\tau) =< \delta\nu(t)\delta\nu(t+\tau) >$,

$$S_{\delta\nu}(\omega) = \int R_{\delta\nu}(\tau)e^{-i\omega\tau}d\tau. \tag{25}$$

The relation between $S_{\delta\nu}(\omega)$ and $I(\omega)$ is given by [18],

$$I(\omega) = E_0^2 \int_0^\infty cos\left[(\omega_0 - \omega)\,\tau\right] exp\left[-4\int_0^\infty S_{\delta\nu}(\omega)\frac{sin^2\left(\omega\tau/2\right)}{\left(\omega/2\pi\right)^2}d\omega\right]d\tau. \tag{26}$$

Diode lasers typically exhibit two types of noise; white frequency noise with a constant PSD, leading to a Lorentzian intensity profile, and flicker frequency noise with a $1/f$ PSD, leading to a Gaussian intensity profile. The combination of the two leads to a Voigt line profile.

White frequency noise This type of noise is characterized by constant power spectral density, $S_{\delta\nu}(f) = h_0$ resulting a Lorentzian lineshape with a $FWHM = 2\pi^2 h_0$.

One example of white frequency noise, which is inherent to all lasers, originates from spontaneous emission in the laser gain medium, enhanced by the resonator cavity, which leads to phase fluctuations of the laser field. Starting with the laser field equations and introducing a Langevin term with a delta-function correlation in time, representing spontaneous emission, one can obtain the constant frequency dependence of the resulting frequency noise PSD [13, 20]. The Lorentzian lineshape can also be directly calculated from the response of the laser to the pumping process [18, 17]. The obtained linewidth, originally calculated by Schawlow and Townes [15], is

$$\Delta\nu = \frac{\pi h \nu_0}{P} \left(\Delta\nu_c\right)^2 , \tag{27}$$

where ν_0 is the lasing frequency, P is the output power of the laser and $\Delta\nu_c$ is the linewidth of the resonator cavity. This value is the quantum limit for laser frequency noise and yields the natural laser linewidth (in the absence of feedback narrowing the line).

Spontaneous emission has an additional contribution to the frequency noise PSD. This contribution is due to the fact that it leads to carrier density fluctuations which in turn give rise to fluctuations in the refractive index of the gain medium and hence change the resonant emission frequency. Two different approaches exist in treating this contribution. In one, the optical spectrum retains the Lorentzian lineshape however broadened [13, 20], whereas in the other the lineshape is modified due to an additional $1/f$ noise PSD [18] as is discussed in the next paragraph.

Flicker frequency noise This type of noise is also known as $1/f$ noise, since the corresponding power spectral density has the form $S_{\delta\nu}(f) = \frac{h_{-1}}{f}$. The optical spectrum obtained under this noise has a Gaussian shape with variance $\sigma^2 = 3.56 h_{-1}$ and hence, $FWHM = 2\sqrt{ln2}\sigma = 3.14\sqrt{h_{-1}}$. It is suggested [18] that the physical origin of this noise lies in fluctuations of the charge carriers density that have a Gaussian statistics. These fluctuations are both due to spontaneous emission in the laser and due to other "technical" sources e.g. fluctuations in the pumping process. As was already mentioned, carriers density fluctuations lead to fluctuations in the refractive index of the gain medium and thus change the laser frequency.

Voigt line profile In order to account for both types of frequency noise, we can treat the charge carriers density, n, as a random variable with Gaussian probability distribution $p(n)$. For each

realization of n, the resonant frequency of the laser is $\omega_0(n)$, and the emission spectrum has a Lorentzian lineshape centered at this value. The resulting lineshape is the convolution of the Lorentzian lineshape with the Gaussian probability distribution for n. The resulting function is called the Voigt function which was shown to give a good quantitative fit to diode lasers spectra [18].

6.2.2 External cavity diode laser (ECDL)

The optical spectrum of bare laser diodes can reach few nanometers (hundreds of GHz) due to simultaneous oscillation of multiple longitudinal resonator modes. For single mode diodes the spectrum is much narrower, typically with a linewidth of hundreds of MHz, but they also may exhibit mode-hopes with the slightest change of temperature or driving current. Also, tuning the laser to an exact atomic transition wavelength, in a stable manner, is very difficult. Stable single mode operation and tunability are achieved by extending the diode laser internal cavity with an additional frequency selective element such as a diffraction grating. A schematic of one such configuration, the "Littrow" configuration, is shown in Fig. 13. A diffraction grating is used to diffract part of the laser beam back into the laser diode and thus close an extended cavity between the grating and the back facet of the diode. The grating acts as a spectral filter and efficiently diffracts only a narrow band of wavelengths in the right direction. Only one external cavity mode, the one that has the largest gain, is selected by the laser. If no AR coating is added on the output facet of the bare diode, the internal resonator of the diode takes part in the selection of the lasing mode. AR coating usually allows for more stable single-mode operation and improves mode-hop free tuning of an ECDL. However it is not always available for a specific wavelength and furthermore, it significantly increases the diode cost. The lasing frequency can be tuned by adjusting the grating angle. For this purpose a PZT is connected to the back of the grating. We use an extra long ECDL, without AR coating (Toptica, model DL100).

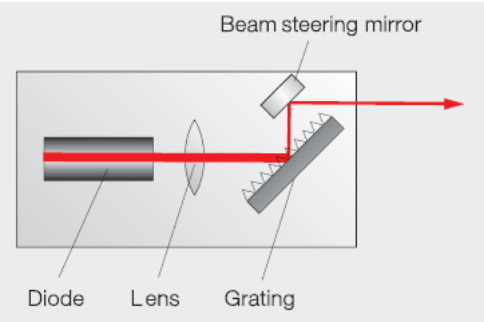

Figure 13: ECDL Littrow design scheme. Diffraction grating is used to diffract part of the laser beam back into the laser diode and thus close an extended cavity between the grating and the back facet of the diode.

Schawlow-Townes linewidth As discussed above, the quantum limit for laser linewidth is given by $\Delta\nu = \frac{\pi h\nu_0}{P}(\Delta\nu_c)^2$. Thus narrowing the linewidth of the resonator cavity decreases the linewidth of the laser. The linewidth of the resonator cavity can be decreased simply by increasing its length (decreasing the $FSR = \frac{c}{2L}$). Since the Finesse, F, of the cavity (dictated by light losses during a round cavity trip) is unchanged, the linewidth $\Delta\nu_c = \frac{FSR}{F}$ decreases as the FSR decreases. Therefore a custom designed extra long cavity $L \simeq 10\,cm$ is used. The theoretical Schawlow-Townes linewidth for our laser parameters is $\Delta\nu \simeq 200\,Hz$ with an external cavity finesse of $F = 1$, cavity length of $L = 10\,cm$ and laser output power $P = 10\,mW$.

6.2.3 Frequency noise characterization and reduction

Acoustic noise isolation The extra long external cavity used to decrease the Schawlow-Townes linewidth, might however increase the susceptibility to acoustic noise. To reduce acoustic noise, the laser-head is mounted on a separate breadboard, well isolated from vibrations and acoustic noise using acoustic foam cover and Sorbothane rubber pads. The cables that lead to the head are fixed to the table to reduce their vibration conductivity.

Initial frequency noise PSD To analyze the frequency noise of the laser before it is locked to the ULE cavity, we use a lower finesse ($F = 750$) Invar cavity. The linewidth of the cavity is $FWHM = 1\,MHz$. A PZT is connected to one of the mirrors of the cavity to control its length and thus its resonant frequency. The cavity is then locked to the laser using a PDH error signal. The feedback to the cavity is performed via the PZT at frequencies $f \lesssim 10\,kHz$ (the mechanical resonance of the PZT is at $f \simeq 13\,kHz$). Since the PDH error signal is linear in the vicinity of the resonance, voltage fluctuations observed on the error signal can be easily translated to frequency fluctuations. Therefore, by inspecting the error signal with an RF spectrum analyzer, the PSD of the frequency noise, at frequencies significantly larger than $10kHz$, can be extracted. The obtained PSD is plotted in Fig. 14. The sharp peaks in the lower frequency range as well as the decrease in the PSD at $f \lesssim 20\,kHz$, are an artifact of the locking. Nonetheless, a flicker noise behavior can be seen at frequencies $f \lesssim 80\,kHz$, and white noise at $f \gtrsim 80\,kHz$. The estimated contribution of the flicker (white) noise to the linewidth is then is $\Delta\nu_{flicker} = 220(80)\,kHz$ ($\Delta\nu_{white} = 1.16(3)\,MHz$), giving a total linewidth of $\Delta\nu = \sqrt{\Delta\nu_{flicker}^2 + \Delta\nu_{white}^2} = 1.18(3)\,MHz$. The linewidth obtained from the white noise component of the PSD does not reproduce the Schawlow-Townes linewidth and is perhaps of different origin.

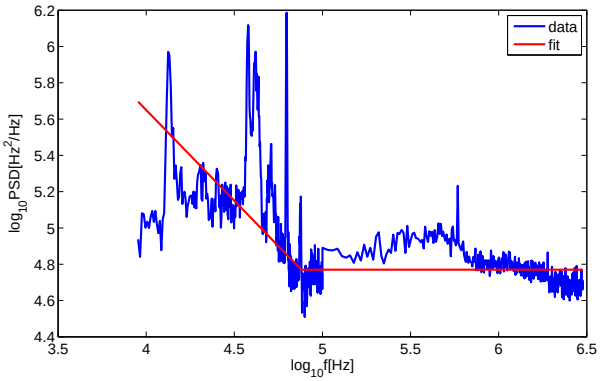

Figure 14: Power spectral density of the laser frequency noise. The sharp peaks in the lower frequency range as well as the decrease in the PSD for $f \lesssim 20\,kHz$, are an artifact of the locking. A flicker noise behavior can be seen at frequencies $f \lesssim 80\,kHz$ with estimated contribution to the linewidth of $\Delta\nu_{flicker} = 220(80)\,kHz$. For frequencies $f \gtrsim 80\,kHz$ the PSD is white, resulting in a linewidth of $\Delta\nu_{white} = 1.16(3)\,MHz$. The total linewidth obtained is $\Delta\nu = 1.18(3)\,MHz$.

Feedback loop The laser is locked to the ULE cavity using a PDH locking scheme [**?**]. This locking method has several advantages: the error signal is not susceptible to amplitude noise, the locking bandwidth is relatively large (in comparison to other laser locking schemes that rely on light which is transferred through the cavity as an error signal)), and the method is not invasive (no additional components in the reference cavity are required, as in the Hänsch–Couillaud method). However, it does require phase modulation at a high frequency, $f_{mod} \simeq 20\,MHz$, which we achieve using an Electro-Optic Modulator (EOM).

The PDH error signal is extracted using a Pound-Drever-Hall Detector (PDD/F) and fed into a Fast Analog Linewidth Control (FALC) PID controller. Both modules are manufactured by Toptica. The output of the FALC is divided into two branches; the limited branch is used for attenuation of high frequency noise, but gives limited gain at low frequencies. This branch is used for feedback via the FET modulation circuit, that allows fast modulation of the laser current ($20\,MHz$ bandwidth). The unlimited branch serves as a full integrator and is used for feedback via the laser PZT. The settings of the FALC are optimized to maximally reduce laser frequency noise PSD and thus also the linewidth of the laser. The locking bandwidth on the unlimited branch is $f \simeq 2\,kHz$, limited by the mechanical resonance of the PZT. This branch is responsible for locking the laser on longer time scales, but is irrelevant for regarding the fast linewidth of the laser. We will concentrate on the fast, limited, branch in the following discussion. For this branch, the locking bandwidth, i.e. the unity gain frequency, is $\simeq 1\,MHz$.

A schematic drawing for the feedback loop of the laser is presented in Fig. 15. Here, i_0 is the set point of the current on the diode, $i(s)$, $f(s)$ and $N(s)$ are the Laplace transforms of the current on the diode laser, the frequency of the laser, and the frequency noise respectively. $H(s)$, $G_{FALC}(s)$ and $G_{FET}(s)$ are the transfer functions of the sensor (PDH error signal), the FALC and the FET

modulation circuit respectively.

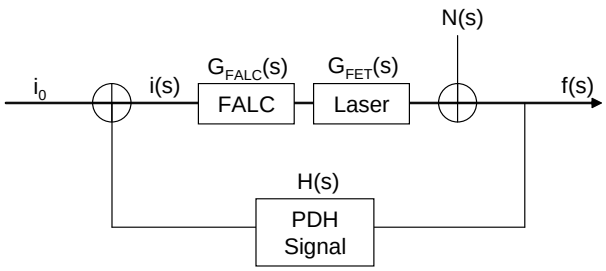

Figure 15: Feedback loop

The closed loop transfer function for the above feedback loop is

$$f = \frac{G}{1+HG} i_0 + \frac{1}{1+HG} N, \tag{28}$$

where $G(s) = G_{FALC}(s) \cdot G_{FET}(s)$. Thus, the noise is attenuated by a factor of $\frac{1}{1+HG}$.

The transfer function of the sensor has two contributions. One from the optical PDH, $H_{PDH}(s)$, and one due to the transfer function of the PDD/F module, $H_{PDD/F}(s)$. The later is assumed to have a bandwidth of $f \gtrsim 3\,MHz$ and is therefore taken to be constant at lower frequencies.

The transfer function for the PDH error signal, for frequencies much lower than the modulation frequency, $f \ll f_{mod} \simeq 20\,MHz$, is given by [2]

$$H_{PDH}(s) = K_{ph} P_0 m \frac{1}{f_p} \frac{1-\xi}{1+\frac{s}{f_p}}, \tag{29}$$

where $f_p = HWHM = 9.67\,kHz$ is the reference cavity Half Width at Half Maximum (HWHM), K_{ph} is the photodiode gain, P_0 is the laser power, m is the EOM modulation index. The corresponding Bode plot is shown in Fig. 16a.

The settings of the FALC used are XSLI=1, SLI=10, FLD=6, FLI=10. A Bode plot for the resulting transfer functions is given in Fig. 16b.

Assuming $G_{FET}(s) = const$ for $f \ll 20\,MHz$, and disregarding any delay in the loop (estimated to give a $\sim 10^\circ$ phase shift at $1\,MHz$), the Bode plot for the overall open loop transfer function is shown in Fig. 16c.

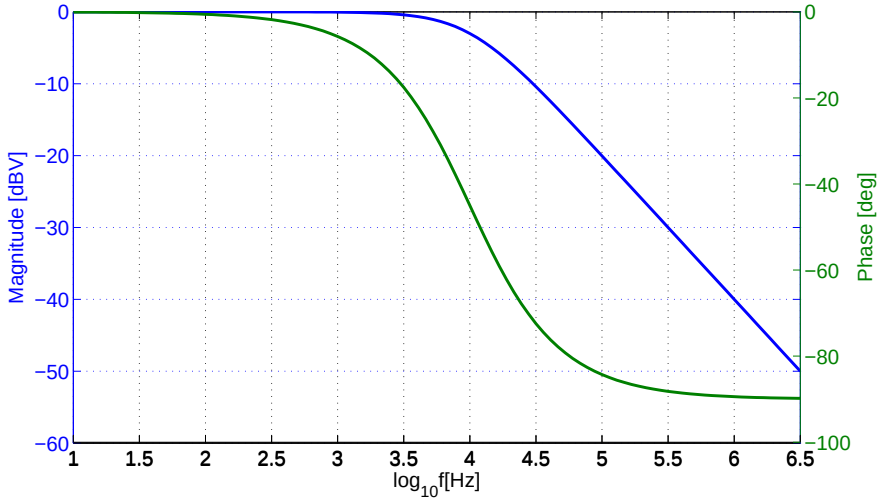

(a)

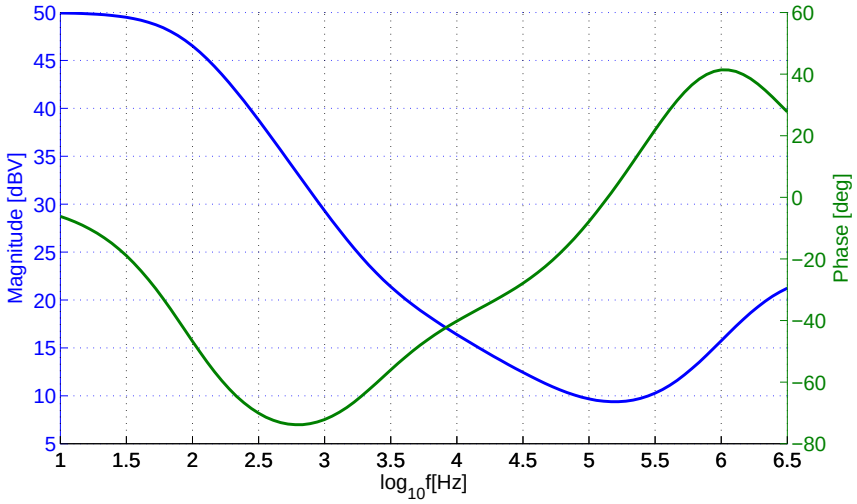

(b)

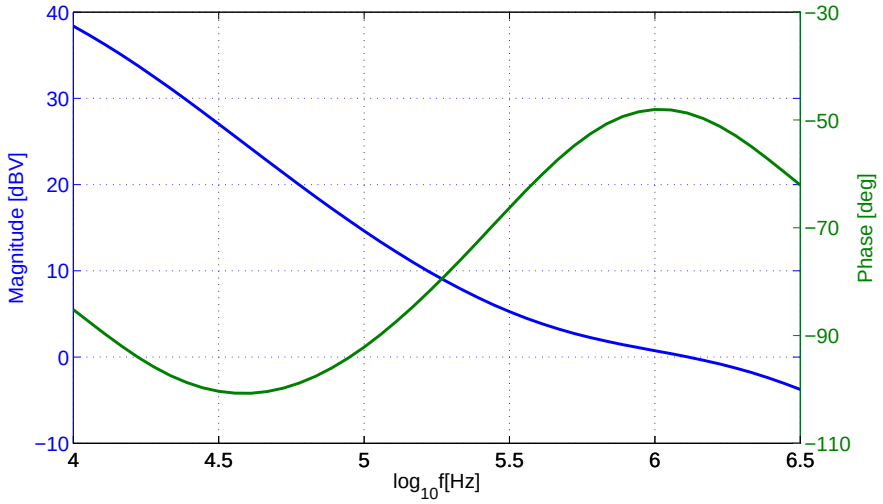

(c)

Figure 16: Bode plots for the transfer functions of the (a) PDH error signal (b) FALC. (c) Overall open loop Bode plot, zooming on the frequency range between $10kHz$ and few MHz. FET transfer function is assumed to be constant and delay in the loop is disregarded.

The Bode plot for the overall transfer function shown in Fig. 16c is inconsistent with the observation of oscillations at $\simeq 1MHz$ as the proportional gain in the loop is increased. This suggests that the transfer function of the FET and/or the PDD/F module is not constant and requires further characterization. However, the magnitude plot predicts $\sim 15\,dB$ attenuation of noise PSD at $f \simeq 100\,kHz$ and $\sim 40\,dB$ attenuation at $f \simeq 10\,kHz$ which is roughly consistent with our measurements as we will show next.

Resulting frequency noise PSD Once the laser is locked, the PSD of the reduced frequency noise can be extracted from the in-loop PDH error signal (on the ULE cavity). Unfortunately a measurement of the laser frequency noise on an independent detector (i.e. out of loop) did not give a reliable result and needs to be improved. The obtained noise PSD is presented in Fig. 17a. The resulting attenuation of the PSD is plotted in 17b. It can be seen that the noise PSD is attenuated by $\sim 20\,dB$ at $f \simeq 100\,kHz$ and $\sim 45\,dB$ at $f \simeq 10\,kHz$, in agreement with the prediction based on the calculated transfer function.

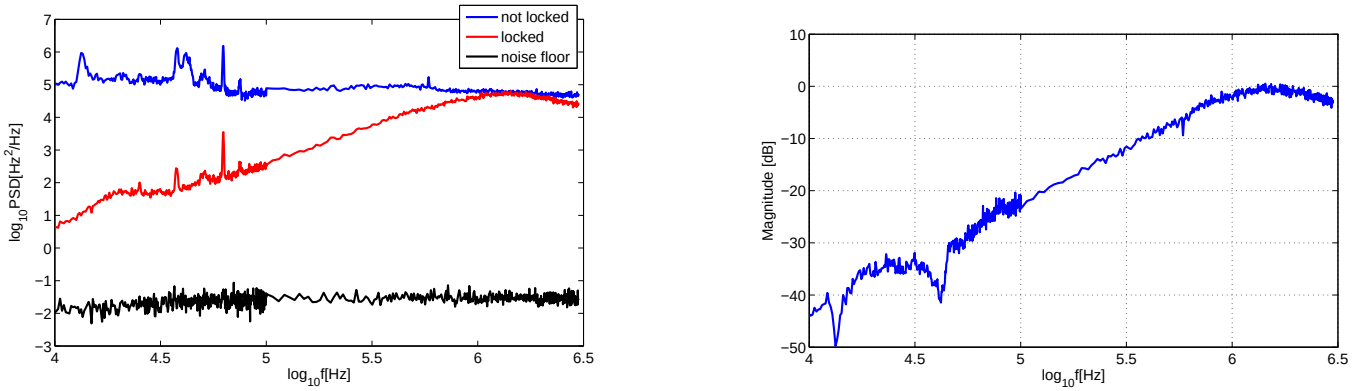

(a) (b)

Figure 17: (a) Frequency noise PSD, before and after the laser is locked. The noise floor of the detector is given for reference. (b) Attenuation of noise PSD. The noise is attenuated by $\sim 20\,dB$ at $f \simeq 100\,kHz$ and $\sim 45\,dB$ at $f \simeq 10\,kHz$

To give an estimate on the fast linewidth of the laser the RMS of frequency fluctuations can be calculated. When the laser is locked, frequency fluctuations RMS, integrated over the bandwidth from $1\,kHz$ to $100\,kHz$ is $\Delta\nu_{RMS} \simeq 3\,kHz$. Given Rabi frequency of $\simeq 50 - 100\,kHz$, frequencies larger than these won't affect the shelving process as they will be averaged over during the π pulse. This is in comparison with $\Delta\nu_{RMS} \simeq 130\,kHz$, over the same bandwidth, before the laser is locked.

6.3 High finesse ultra low expansion (ULE) cavity

The stabilization of the laser frequency and the narrowing of its linewidth is achieved by locking the laser to a high finesse ULE cavity. The cavity was made by Advanced Thin Film, Boulder

according to a JILA (Jun Ye's group) design [9]. To decouple the principle vibration mode of the cavity from acoustic vibrations of the mount, the cavity is vertically mounted on the node of the mode, as can be seen in Fig. 18. In addition, the mount is isolated from the cavity using viton rubber pads. The mirrors are optically bonded to the cavity, to prevent using glues.

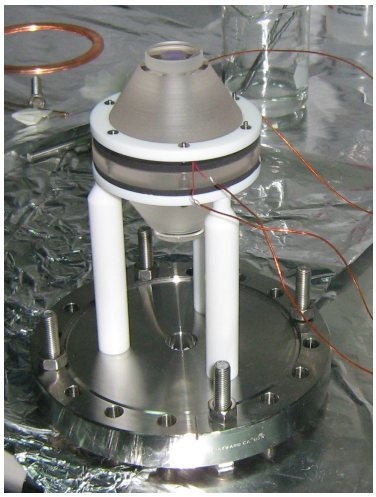

Figure 18: Photo of the ULE cavity. The cavity is mounted vertically on the node of the principle vibration mode, to decouple the mode from acoustic vibrations of the mount. In addition, the mount is isolated from the cavity using viton rubber pads.

The cavity is plano-concave and has a length of $L = 77.5\,mm$. The FSR for the cavity longitudinal modes is $1.93GHz$, and the width of each mode is $FWHM = \frac{FSR}{F} = 19.3kHz$. The cavity is placed in vacuum to prevent intra-cavity air density changes from drifting the cavity resonance. To reach a finesse of $F = 10^5$, mirrors of very high reflectivity are used. The vacuum also ensures that the reflectivity of the mirrors is not damaged.

When the frequency of the laser is swept fast over the cavity resonance, ringdown of the transmission signal is observed (Fig. 19). A ringdown time of the cavity is measured to be $\tau = 7.0(1)\mu s$ corresponding to a cavity linewidth of $\Delta\nu = 22.7(3)kHz$.

The ULE glass used as the cavity spacer has a very low thermal expansion coefficient typically on the order of $10^{-8}\frac{1}{K}$. This is important for long term stability of the laser frequency with respect to the atomic transition frequency. Once the laser is locked to the cavity and the $S_{1/2} \rightarrow D_{5/2}$ transition monitored on the ion, the thermal expansion coefficient can be measured. The cavity thermal expansion coefficient determines the amount by which its relative length changes vs. temperature. A change in the cavity length leads to a change in the resonance frequency of the cavity, $\frac{\Delta f}{f} = -\frac{\Delta L}{L}$. Since the laser is locked to the cavity, its frequency changes accordingly. A different AOM frequency is then required to observe the transition on the ion. Figure 20 shows the frequency of the AOM at resonance with the $S_{1/2} \rightarrow D_{5/2}$ transition vs. the temperature recorded by a thermistor, placed inside the vacuum chamber on the cavity mount. The thermal expansion

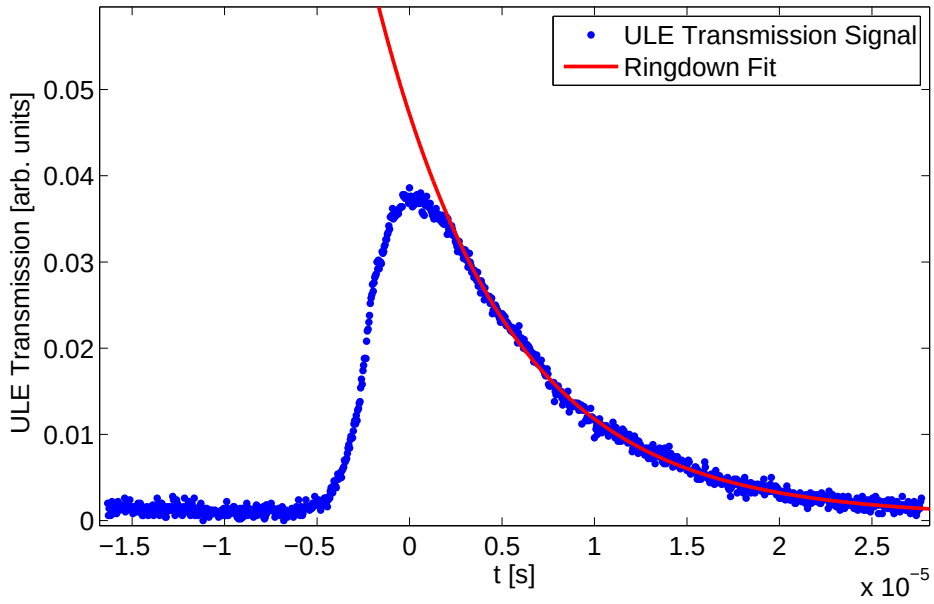

Figure 19: ULE cavity ringdown signal. Ringdown time is $\tau = 7.0(1)\mu s$ corresponding to cavity linewidth of $\Delta\nu = 22.7(3)kHz$.

coefficient extracted from this measurement is indeed $\alpha \simeq 10^{-8}\frac{1}{K}$. The positive α value indicates that by somewhat reducing the working temperature of the cavity the value of α will be reduced as well.

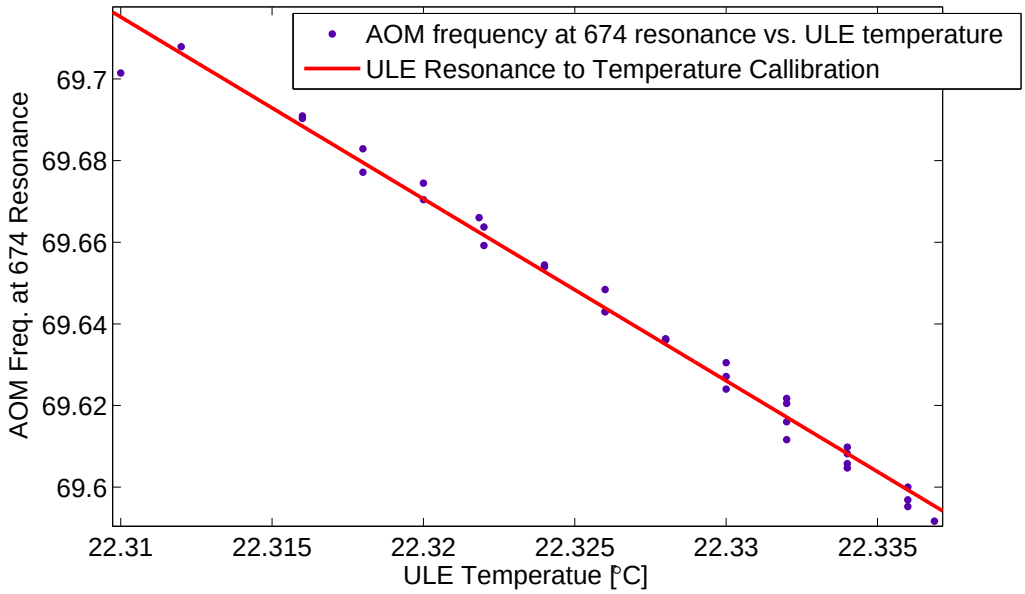

Figure 20: ULE thermal drift. The thermal expansion coefficient extracted is $\alpha \simeq 10^{-8}\frac{1}{K}$.

6.4 Intensity stabilization

Intensity fluctuations of the 674 nm light lead to fluctuations in the Rabi frequency, and therefore affect shelving efficiency. The origin of intensity noise is mainly in fiber phase noise, translated to AM noise when passing through a polarizing beam splitter (PBS) on the way to the ion. To prevent this, the intensity of the light on the ion need to be stabilized. The feedback loop on the intensity is presented in Fig. 11. The intensity of the laser on the ion is monitored and controlled via the RF power of the acousto-optic modulator (AOM) switch. Decreasing the RF power on the AOM decreases the diffraction efficiency and thus reduces the intensity of the diffracted light. The set point for intensity locking can be regulated from the computer.

7 Electron shelving

The $S_{1/2} \rightarrow D_{5/2}$ transition lines are observed by scanning the AOM frequency and performing electron shelving followed by fluorescence measurement. If the frequency of the laser is close to the frequency of one of the transitions, the electron is shelved with some probability. If the electron is shelved, no scattered photons are detected. Therefore, the fraction of dark events corresponds to the shelving probability and serves as a measure for population inversion.

A technical note is that the -1^{st} diffraction order of the AOM is used. Therefore when the frequency of the AOM is increased, the frequency of the laser light seen by the ion is decreased.

7.1 Laser frequency scan

The shift in frequency due to Zeeman splitting is

$$\Delta f\,(m, m') = \left(-2.802\frac{MHz}{G} \cdot m + 1.680\frac{MHz}{G} \cdot m'\right) \cdot B \tag{30}$$

Here the first (second) term is due to the Zeeman splitting of the $D_{5/2}$ ($S_{1/2}$) manifold. The resulting frequencies for all possible transitions are shown in Fig. 21. The allowed transitions for the geometrical configuration used in the experiment are indicated in red.

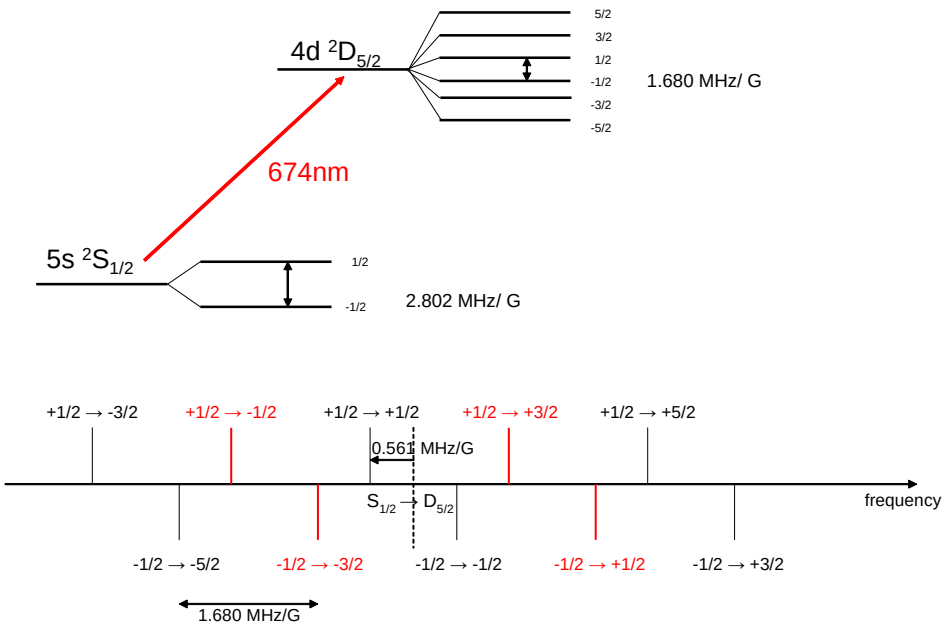

Figure 21: $S_{1/2,m} \rightarrow D_{5/2,m'}$ frequency shifts. Geometrically allowed transitions are marked in red.

In the absence of optical pumping to one of the Zeeman split levels of $S_{1/2}$, the ion can be in either of the two spin states. Hence all the four transitions $S_{1/2,-1/2} \rightarrow D_{5/2,-3/2}$, $S_{1/2,-1/2} \rightarrow D_{5/2,+1/2}$, $S_{1/2,+1/2} \rightarrow D_{5/2,-1/2}$, $S_{1/2,+1/2} \rightarrow D_{5/2,+3/2}$ with non-zero matrix element can be observed. A result of AOM frequency scan is given in Fig. 22. The variation in the shelving efficiency (i.e. the corresponding fraction of dark events) on the different transitions is due to the difference in the corresponding Rabi frequencies, resulting form the geometrical factors in the transition matrix elements and the variation in laser light intensity as function of AOM frequency.

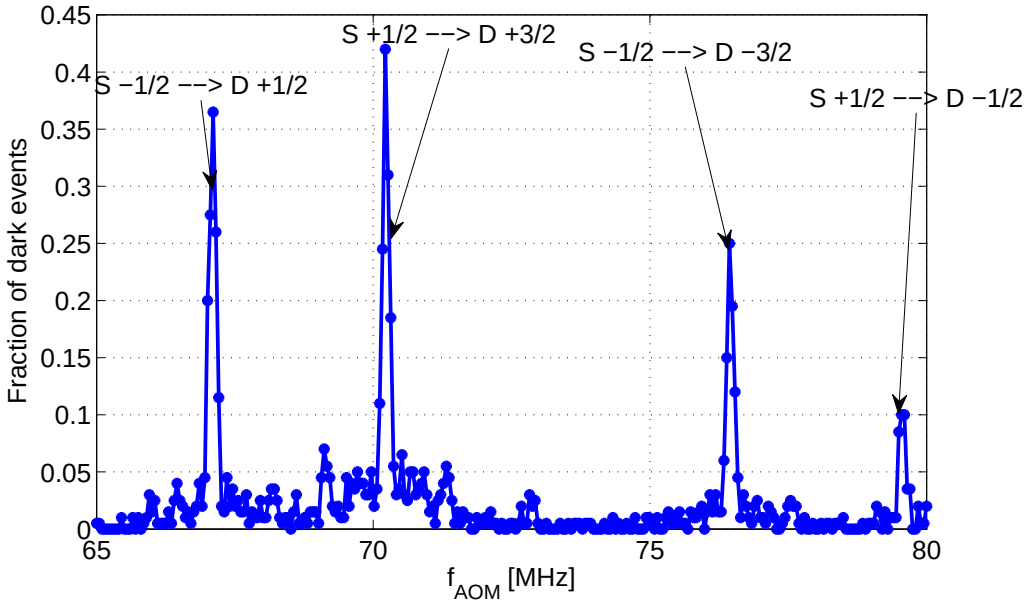

Figure 22: The four $S_{1/2} \rightarrow D_{5/2}$ transition lines corresponding to $\Delta m = \pm 1$ quadruple transitions.

A higher resolution frequency scan of the $S_{1/2,1/2} \rightarrow D_{5/2,3/2}$ transition is shown in Fig. 23. Here the motional sidebands can be clearly observed. Including first and second order sidebands, the theoretical population inversion is given by

$$P_{dark} = A \left\{ \sum_{\Delta n=-2}^{2} \frac{\Omega_{n,n+\Delta n}^2}{\Omega_{n,n+\Delta n}^2 + 4\pi^2 \left(f - f_{\Delta n}\right)^2} sin^2 \left(\frac{\sqrt{\Omega_{n,n+\Delta n}^2 + 4\pi^2 \left(f - f_{\Delta n}\right)^2}}{2} t_\pi \right) \right\} + c. \quad (31)$$

Here $\Omega_{n,n+\Delta n}$ denote the Rabi frequencies on the carrier, the first, and the second order sidebands. The resonant frequencies of the carrier and sidebands are denoted $f_{\Delta n}$. The duration of the pulse is t_π. A fit to Eq. 31 yields a Rabi frequency $\Omega_{n,n} = (2\pi)57\, kHz$ on the carrier, sideband Rabi frequency $|\Omega_{n,n-1}| = \Omega_0 \eta \sqrt{\bar{n}} = (2\pi)\, 12\, kHz$ and a mean harmonic oscillator level of $\bar{n} \simeq 3$.

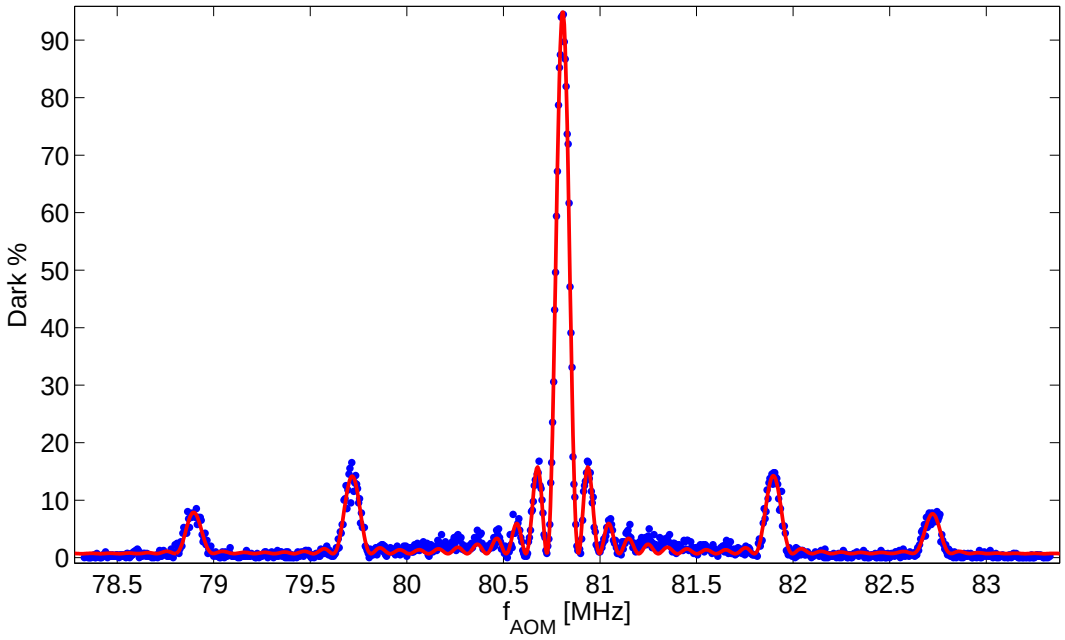

Figure 23: $S_{1/2,1/2} \rightarrow D_{5/2,3/2}$ carrier transition and motional sidebands. The fit presented yields a carrier Rabi frequency $\Omega_{n,n} = (2\pi)57\,kHz$, pulse duration $t = 10\,\mu s$ and a mean harmonic oscillator level $\bar{n} \simeq 3$.

7.2 Pulse duration scan

A time scan of a resonant $674nm$ laser pulse is shown in Fig. 24. A fit to Eq. 14 yields a Rabi frequency of $\Omega_0 = (2\pi)\,74.2(2)\,kHz$ and a mean harmonic level number $\bar{n} \simeq 2.7(2)$.

7.3 Ramsey experiments

The coherence time of operations on the ion is governed by relative frequency fluctuations between the laser and the atomic transition, due to magnetic field fluctuations and laser linewidth of the laser. The most dominant component of magnetic field noise is at $50\,Hz$. This noise component is significantly attenuated when the experiment is repeated with an AC line trigger. In this mode of operation dephasing due to magnetic field noise is negligible and hence dephasing time and dynamics provide an estimate for the laser linewidth.

Figure 25a shows the results of a Ramsey experiment on the $S_{1/2,1/2} \rightarrow D_{5/2,3/2}$ transition. In the experiment two $\pi/2$ pulses are applied with a variable time τ_{Ramsey} between them. The laser is detuned by $\Delta = 50\,kHz$ from resonance. The relative phase between the two pulses (in the rotating frame) is cycled by 2π every time τ_{Ramsey} is scanned through an integer multiple of $\frac{1}{\Delta}$, resulting in fringes in the fraction of dark events. Fringe visibility falls as the coherence between

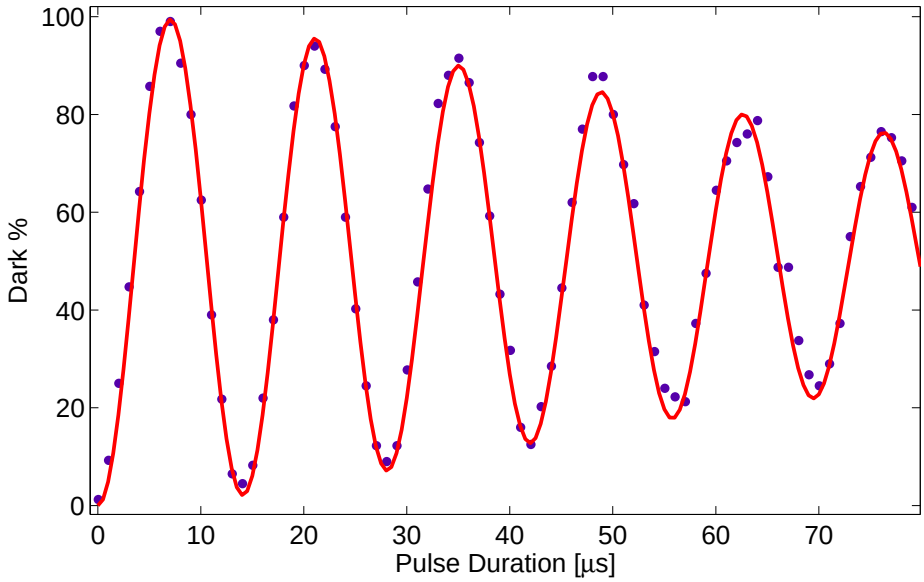

Figure 24: $S_{1/2,1/2} \rightarrow D_{5/2,3/2}$ pulse duration scan. The fit presented yields a Rabi frequency of $\Omega_0 = (2\pi)\,74.2(2)\,kHz$ and a mean harmonic level number $\bar{n} \simeq 2.7(2)$.

the two pulses is lost. In the experiment the visibility falls to $\simeq 40\%$ (half of the initial value) after time of $\tau_{coh,optical} \simeq 700\,\mu s$.

To estimate the contribution of magnetic field noise to dephasing the same experiment is performed on the Zeeman $S_{1/2,+1/2} \rightarrow S_{1/2,-1/2}$ transition, using an RF field to apply the $\pi/2$ pulses. The result is shown in Fig. 25(b). The time over which fringe visibility falls to half of its initial value is $\tau_{coh,Zeeman} \simeq 1\,ms$. The magnetic susceptibility is larger by a factor of 2.5 for the $S_{1/2}$ Zeeman transition than for the optical qubit above. The two noise contributions, due to magnetic field fluctuations and laser frequency noise, are statistically independent and therefore can be quadratically subtracted.

Thus the measured coherence time of $\tau_{coh,optical} \simeq 700\,\mu s$ has an estimated contribution from a laser linewidth $\Delta\nu \simeq \sqrt{\left(\frac{1}{\tau_{coh,optical}}\right)^2 - \left(\frac{1}{\tau_{coh,Zeeman}}\right)^2} \simeq 1\,kHz$.

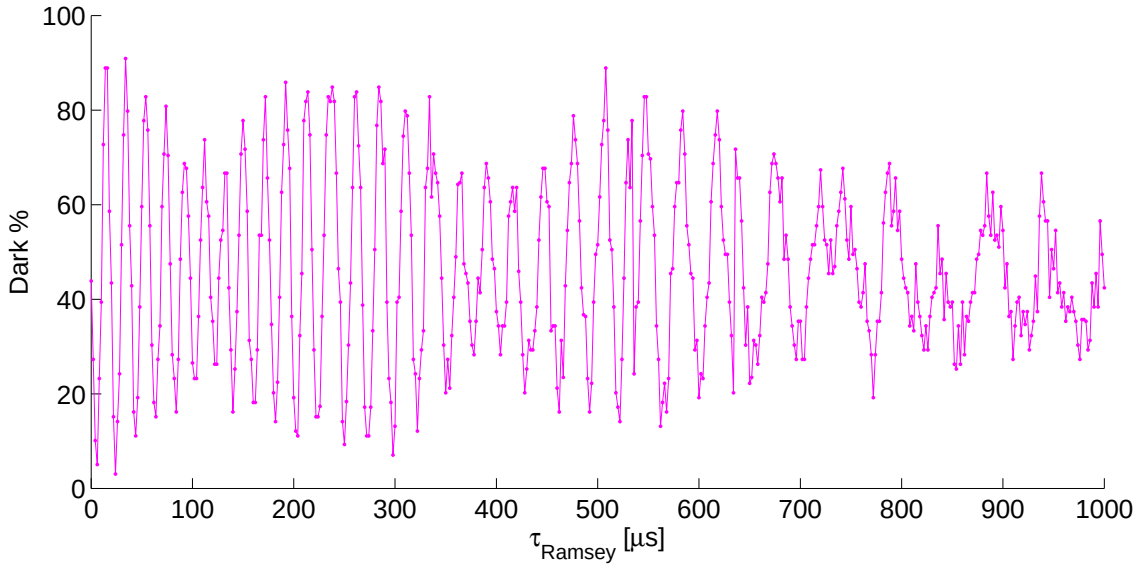

(a)

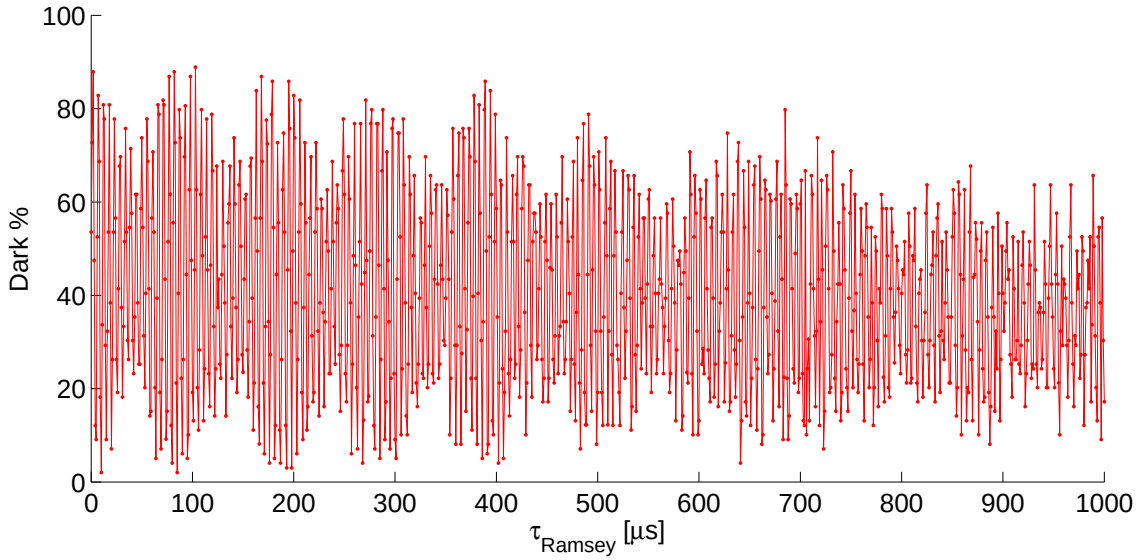

(b)

Figure 25: Ramsey time scan for (a) the optical qubit and (b) the Zeeman qubit. Coherence times of $\tau_{coh,optical} \simeq 700\,\mu s$ and $\tau_{coh,Zeeman} \simeq 1\,ms$ are observed for the optical and Zeeman qubits respectively.

In a similar experiment the frequency of the laser is scanned, while the time between the two $\pi/2$ pulses, τ_{Ramsey}, remains fixed.

This operation is modeled by a multiplication of three rotation matrices. All operations are described in the rotating frame. First, due to interaction with the laser, the Bloch vector is rotated by angle $\theta_{Rabi} = \sqrt{\Omega_0^2 + (2\pi\delta)^2}t_{\pi/2}$ around the Rabi vector direction, $\vec{n}_{Rabi} = \frac{(\Omega_0,0,2\pi\delta)}{\sqrt{\Omega_0^2+(2\pi\delta)^2}}$.

Then, due to laser detuning, the Bloch vector precesses around the $\hat{z}$ axis for a time τ_{Ramsey}. The total precession angle is $\phi_{Ramsey} = 2\pi\delta\tau_{Ramsey}$. Finally, another $\pi/2$ pulse is applied and the Bloch vector is again rotated by θ around $\vec{n}_{Rabi}$. Hence the three rotations are represented by

$$\hat{R} = e^{i\frac{1}{2}\vec{\sigma}\cdot\vec{n}_{Rabi}\theta_{Rabi}} e^{i\frac{1}{2}\vec{\sigma}\cdot\hat{z}\phi_{Ramsey}} e^{i\frac{1}{2}\vec{\sigma}\cdot\vec{n}_{Rabi}\theta_{Rabi}}. \tag{32}$$

The $S_{1/2}$ and $D_{5/2}$ qubit levels are represented by $|\downarrow\rangle = \begin{pmatrix} 0 \\ 1 \end{pmatrix}$ and $|\uparrow\rangle = \begin{pmatrix} 1 \\ 0 \end{pmatrix}$ respectively. If initially the population is entirely in the $S_{1/2}$ level, the population inversion after the operation is given by $\left|\langle\uparrow|\hat{R}|\downarrow\rangle\right|^2$. The affect of harmonic level thermal occupation distribution on the population inversion probability is similar to the one described in section 3.3.4 in the context of simple Rabi flopping.

Figure 26 shows the results of a frequency scan for $\tau_{Ramsey} = 20\,\mu s$ and $50\,\mu s$ together with a fit to the theoretical population inversion curve. Near the resonance, clear fringes with 80% and 70% visibility respectively are observed.

Figure 27 shows the result of a frequency scan near resonance for $\tau_{Ramsey} = 500\,\mu s$. Fringe visibility is still high, $\simeq 65\%$, signifying a coherence time $\tau_{coh} > 500\,\mu s$. The expected oscillation period of these oscillations is $\frac{1}{\tau_{Ramsey}} = 2\,kHz$. The period observed, however, is $\Delta f \simeq 1.5\,kHz$ as can be seen from the fit in the figure. This difference is explained when we take into account the frequency drift of the ULE resonance due to temperature drift as was discussed in section 6.2. A linear drift of $\simeq 0.5\,kHz$ per cycle is then required. Each fringe in the figure is obtained from 7-8 measurement points. Each point is an average over 200 experiments. Since the experiments are AC line triggered, each experiment takes $20\,ms$. Thus the scan of each fringe takes $\simeq 30\,sec$. A drift of $0.5\,kHz$ per fringe corresponds to a drift of $1\,kHz$ in $60\,sec$, equivalently $100\,kHz$ in $100\,min$, or in terms of temperature drift - a change of$\simeq 0.02°C$ over $100\,min$. This result can be directly compared to Fig. 20, showing a drift of $\simeq 100\,kHz$ in $\simeq 90\,min$.

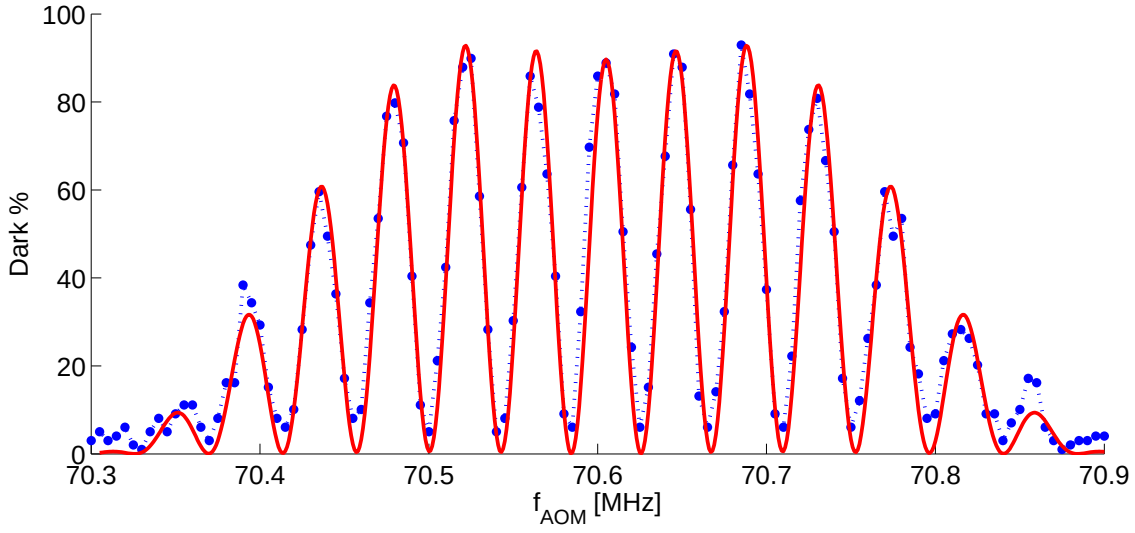

(a)

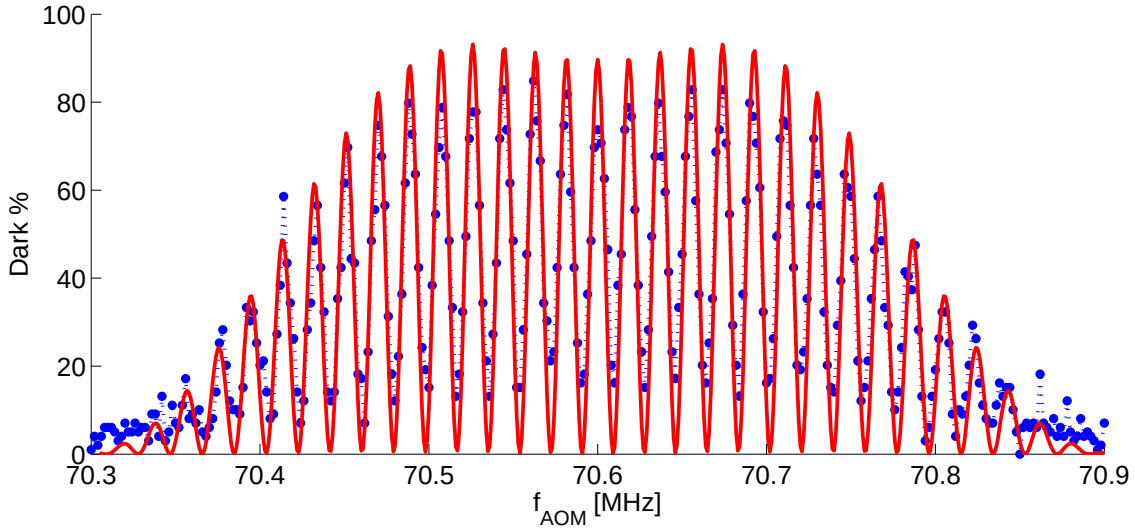

(b)

Figure 26: Ramsey frequency scans on the $S_{1/2,+1/2} \rightarrow D_{5/2,+3/2}$ transition. Ramsey time is fixed at (a) $\tau_{Ramsey} = 20\,\mu s$ and (b) $\tau_{Ramsey} = 50\,\mu s$. The fits presented yield a carrier Rabi frequency $\Omega = (2\pi)103\,kHz$, $\pi/2$ pulse duration $t = 3.1\,\mu s$ and a mean harmonic oscillator level $\bar{n} = 11$.

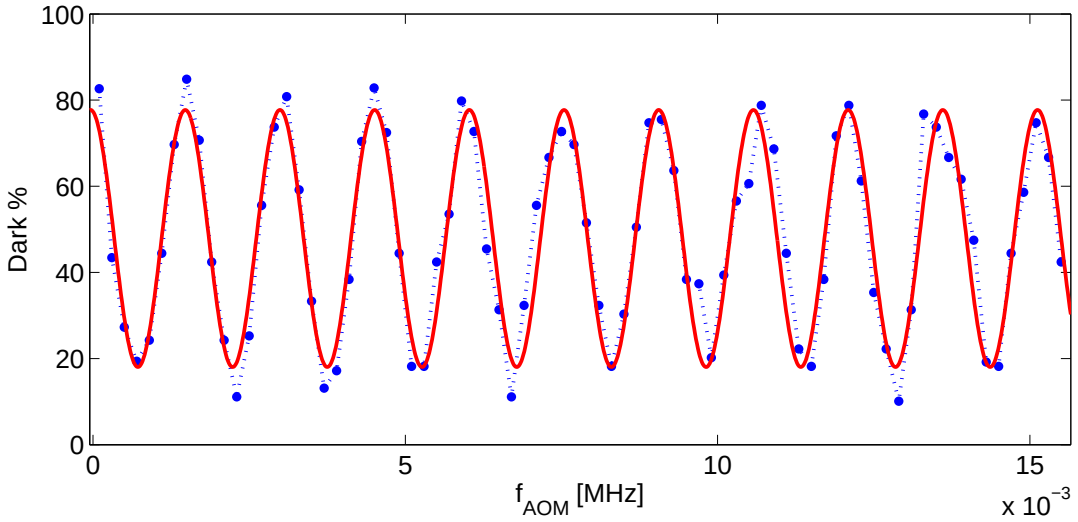

Figure 27: Ramsey frequency scan on the $S_{1/2,+1/2} \rightarrow D_{5/2,+3/2}$ transition. Ramsey time of $\tau_{Ramsey} = 500\,\mu s$ is fixed. A phenomenological decrease of contrast was allowed in the fit. Obtained fringe visibility of $\simeq 60\%$ indicates coherence time $\tau_{coh} > 500\,\mu s$.

8 State detection fidelity

8.1 State preparation and detection

In the experiment, two sets of data are taken. In each set the ion is prepared in one of the two qubit states $|\uparrow\rangle$ or $|\downarrow\rangle$ and then state detection is performed. The preparation and detection of the two qubit states is performed according to the laser pulse sequences presented in Fig. 28. Each set of data contains 10^6 repetitions of the experiment.

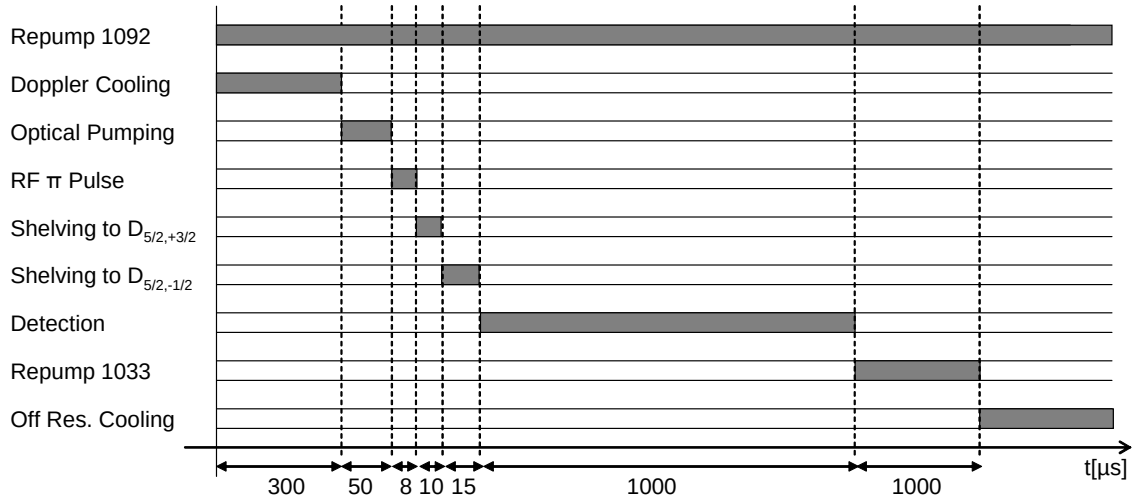

(a)

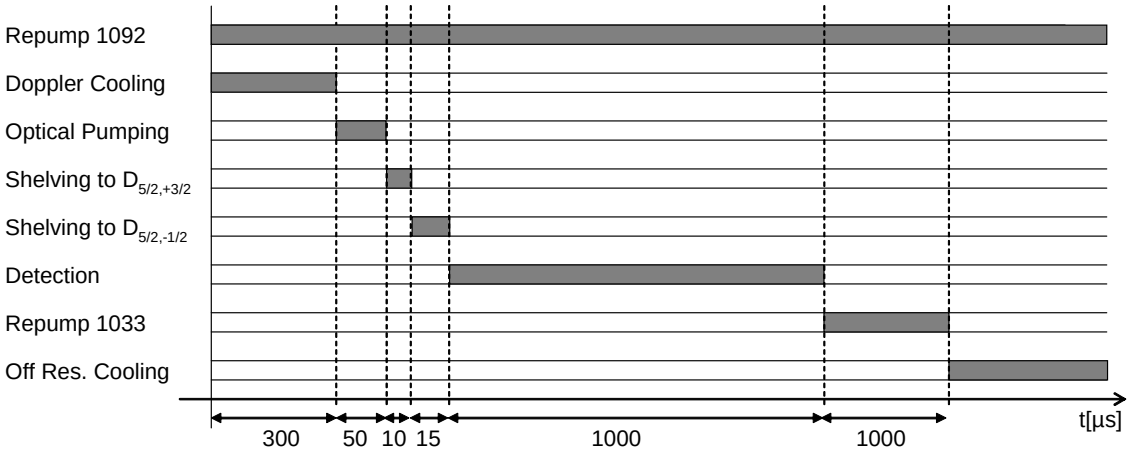

(b)

Figure 28: State preparation and detection laser pulse sequences (a) for the $|\uparrow\rangle$ state and (b) for the $|\downarrow\rangle$ state.

In both sequences the ion is first Doppler cooled for 300 μs. Then state preparation is performed. For both qubit states, state preparation begins with optical pumping to the $|\uparrow\rangle$ state using right circularly polarized (σ^+) 422 nm light, as explained in 3.3.2, for 50 μs. For the $|\downarrow\rangle$ qubit state, optical pumping to the $|\uparrow\rangle$ state is followed by a 8 μs RF π pulse bringing the electron to the $|\downarrow\rangle$ qubit state. State detection starts with electron shelving. A 10 μs π pulse on the $|\uparrow\rangle \rightarrow D_{5/2,+3/2}$ transition is applied. To increase shelving efficiency another 15 μs π pulse is applied on the $|\uparrow\rangle \rightarrow D_{5/2,-1/2}$ transition. Following shelving, an on resonance 422 nm laser light is shined on the ion for a duration of 1 ms for fluorescence detection. During this period photons are collected by the PMT and their time of arrival is recorded for further analysis. Then, population shelved to the $D_{5/2}$ level (if any) is repumped back to the ground state using the 1033 nm laser for 1 ms. At the end of the sequence, an off resonant red detuned 422 nm light cools the ion until the next sequence begins. During the entire sequence the 1092 nm laser is left on to repump population from the $D_{3/2}$ metastable level.

8.2 State detection analysis

8.2.1 Distributions parameters estimation

The obtained histograms, for detection time of 380μs are shown in Fig. 29. A maximum likelihood fit to the expected distributions, given by Eqs. 20a and 20b for the $|\downarrow\rangle$ and $|\uparrow\rangle$ qubit states respectively, is performed. Known detection time $t_{det} = 380\mu s$ and $D_{5/2}$ level lifetime $\tau = 390ms$[8] are used to fit the dark distribution.

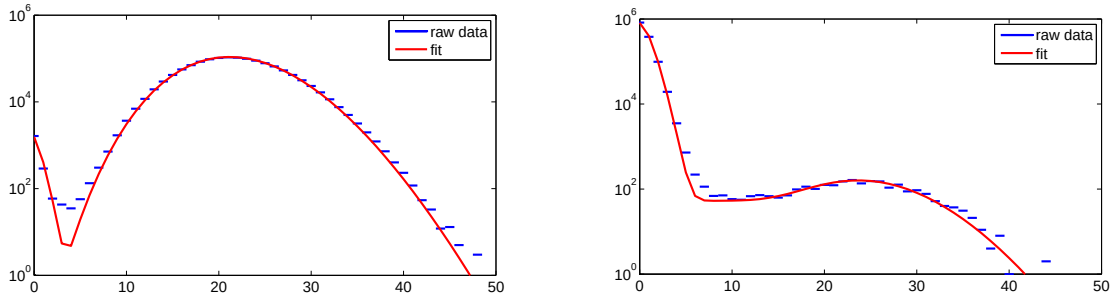

(a) (b)

Figure 29: Measured photon number histograms for qubit initialized in (a) $|\downarrow\rangle$ state and (b) $|\uparrow\rangle$ state

The fit for bright distribution yields initialization and shelving error of $\epsilon_{b,tot} = 1.59(7)\cdot 10^{-3}$, bright photon detection rate $R_b^b = 57.05(2)kHz$ and dark photon detection rate $R_d^b = 0.68(6)kHz$. The fit for dark distribution yields initialization and shelving error of $\epsilon_{d,tot} = 1.24(7)\cdot 10^{-3}$, bright photon detection rate $R_b^d = 65(1)kHz$ and dark photon detection rate $R_d^d = 1.294(3)kHz$. The lower

photon detection rates for the bright data set are due to a lower laser power of the on resonance 422 nm laser used for detection, resulting from a different duty cycle of the acousto-optic modulator used to switch the beam.

8.2.2 Error calculation using cutoff method

The minimal state detection error and optimal parameters required to obtain it can be found based on the measured photon number distributions for the bright and dark states. A contour plot for the mean error as function of the detection time t_{det} and the cutoff on the number of photons n_c, based on the experimental data is shown in Fig. 30a. For comparison, the estimated error, based on the theoretical distributions with parameters found from the fit is shown in Fig. 30b.

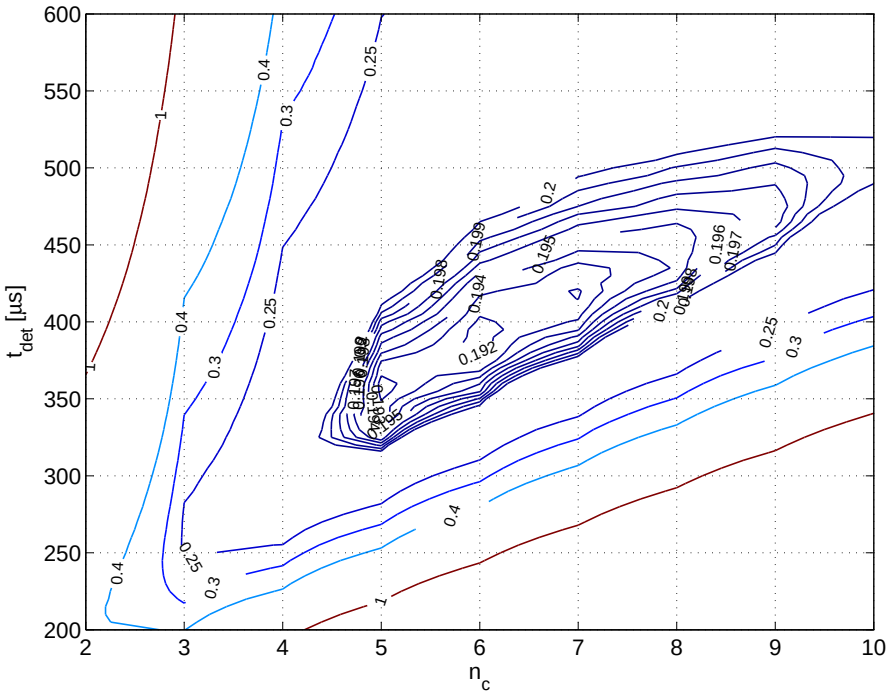

(a)

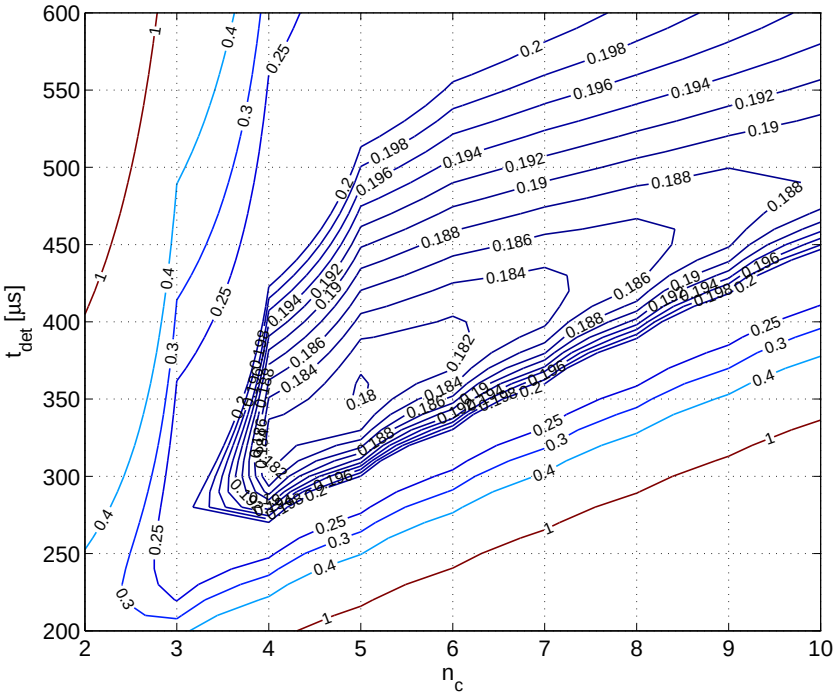

(b)

Figure 30: Contour plots for the state detection error as function of the detection time t_{det} and the cutoff on the number of photons n_c. (a) Based on the experimental data sets. The minimal error is $\epsilon = 1.9 \cdot 10^{-3}$, obtained at $t_{det} = 380\mu s$, $n_c = 6$. (b) Based on the theoretical PDFs with parameters obtained from a fit to experimental data. The minimal error is $\epsilon = 1.8 \cdot 10^{-3}$, obtained at $t_{det} = 350\mu s$, $n_c = 5$.

It can be seen that the overall dependence of the error on the detection parameters based on the theoretical PDFs reproduces quite well the experimental data. Also, the predicted value for the minimal state detection error differs by only $\sim 5\%$ with respect to the experimental value, even though the optimal parameters required to obtain it are slightly shifted. However, the value obtained above for the state detection error is not accurate, due to the different detection rates in the two sets of data. An estimate for the correct error can be obtained using the fitted theoretical distributions, with the change of the detection rates in the bright distribution to be equal to the detection rates in the dark distribution. A contour plot for the error estimated this way is given in Fig. 31.

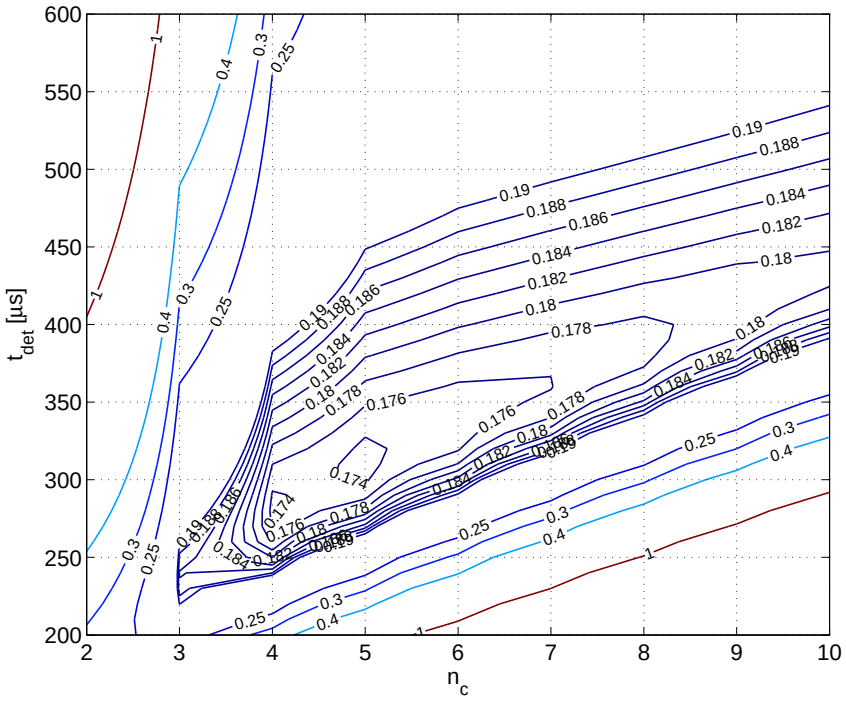

Figure 31: Contour plot for the state detection error as function of the detection time t_{det} and the cutoff on the number of photons n_c based on the theoretical PDFs with parameters obtained from a fit to experimental data, corrected to have the same photon detection rates. Here, the minimal error is $\epsilon = 1.7 \cdot 10^{-3}$, obtained at $t_{det} = 310\mu s$, $n_c = 5$.

It can be seen that the minimum is shifted to a lower detection time $t_{det} = 310\mu s$ yet the same cutoff value $n_c = 5$, and the value of the error at minimum is decreased by $\sim 10^{-4}$ to a value of $\epsilon = 1.7 \cdot 10^{-3}$. Even though the optimal parameters are somewhat different, this does not have a dramatic effect on the detection error.

8.2.3 Photon arrival times

State detection using the likelihood method, described in section 4.2, was performed as well. Figure 32 gives an example of an event that would have been identified as bright using the cutoff method, whereas the likelihood method correctly identifies it as dark. For detection time of $t_{det} = 380\mu s$ the obtained state discrimination error was $\epsilon = 1.8 \cdot 10^{-3}$. That is, an improvement of 10^{-4} with respect to the cutoff method, as expected.

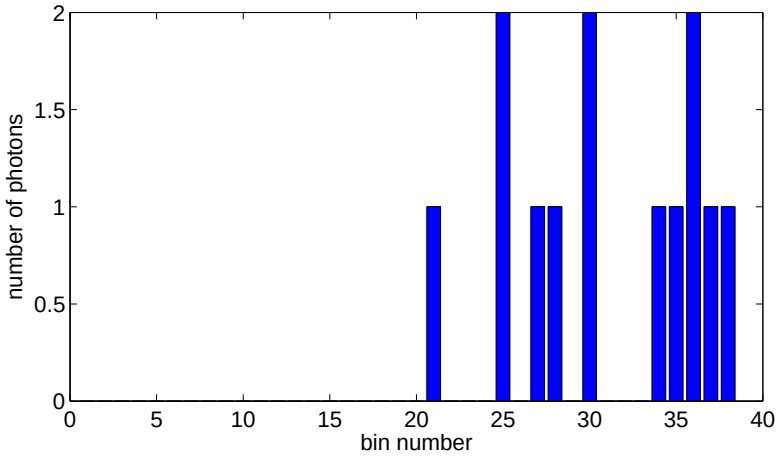

Figure 32: An example of an experiment identified as bright using the cutoff method and as dark using the likelihood method

8.3 Error budget

Obtained detection error of $\epsilon = 1.9 \cdot 10^{-3}$ arises from the combination of initialization and shelving faults with the error due to finite lifetime of the shelved state. The fits to photon counts distributions allowed us to distinguish between these two errors and obtain a value of $1.2 \cdot 10^{-3}$ and $1.6 \cdot 10^{-3}$ for the sum of initialization and shelving errors of the dark and bright states respectively. The following error budget tries to estimate the contribution of different error sources affecting initialization and shelving errors for each of the qubit states.

8.3.1 Initialization errors

Optical pumping Ideally the optical pumping beam has to match a perfect σ^+ polarization. Otherwise, the matrix elements for the $S_{1/2,+1/2} \rightarrow P_{1/2,\pm 1/2}$ transitions will not be zero, and population will be pumped out of the $S_{1/2,+1/2}$ level. To this end the wave-vector, $\vec{k}$, of the beam has to be exactly parallel to the external magnetic field defining the qubit quantization axis and a perfectly circularly polarized beam is required.

First, assume that the propagation direction of the beam is parallel to the quantization axis, but the polarization vector has a σ^- component, $\vec{\epsilon} = \frac{1}{\sqrt{2(1+\epsilon^2)}}\left[(\hat{x}+i\hat{y})+\epsilon\,(\hat{x}-i\hat{y})\right]$. Steady state population of the $S_{1/2,\pm 1/2}$ levels will be determined by the ratio between the matrix elements squared $\left(\frac{\Omega_{S_{1/2,+1/2}\to P_{1/2,-1/2}}}{\Omega_{S_{1/2,-1/2}\to P_{1/2,+1/2}}}\right)^2 = \epsilon^2$. This is also the ratio between the intensities of the two polarization components. To create a σ^+ polarization, 422 nm laser beam is first passed through a wallaston polarizer. The outcoming linearly polarized beam is turned into a circularly polarized one as it passes through a $\frac{\lambda}{4}$ plate. Finally, the beam passes through the vacuum chamber window on its way to the ion. The purity of the linearly polarized beam passing a wallaston polarizer (i.e. the ratio between the intensities of the two polarization components) is typically 10^{-5}. For the imperfectness of the $\frac{\lambda}{4}$ plate, we do not have a quantitative estimate. However, the stress induced birefringence of the vacuum chamber reduces the purity of the polarization of the beam down to $\simeq 10^{-3}$.

When the wave-vector of the beam is not strictly parallel to the ion's quantization axis, the beam will have a π polarization component and induce transitions between $S_{1/2,+1/2} \to P_{1/2,+1/2}$. Denote the angle between the wave-vector, $\vec{k}$, and the magnetic field by θ. The projection of the electric field on the quantization axis is $\frac{E_0}{\sqrt{2}}\theta$ for small θ, leading to a steady state population ratio $\simeq \frac{\theta^2}{2}$. In the experiment the angle of the magnetic field can be adjusted with resolution of $\sim 1^\circ$ with the use of the horizontal and vertical coils. For an angle $\theta = 1^\circ$, the ratio in steady state population is $\simeq 3 \cdot 10^{-4}$.

Taking into account all error sources mentioned above, we estimate the initialization error due to optical pumping to be of the order of 10^{-3}.

RF π pulse To prepare the qubit in the $|\downarrow\rangle$ state the ion is first initialized in the $|\uparrow\rangle$ state via optical pumping and then an RF π pulse is applied. This results in an additional state preparation error of $\sim 10^{-4}$ estimated by measuring the accumulated error of applying multiple π pulses. This way of state initialization is preferred since it is robust, ads a small error with respect to the total error and does not require any manual adjustments (i.e. is computer controlled). An alternative way to prepare the qubit in the $|\downarrow\rangle$ state is by inverting the polarization of the 422 nm laser light used for optical pumping (from σ^+ to σ^-) by rotating a $\frac{\lambda}{4}$ plate used to create the circular polarization. To this end manual adjustment of the wave-plate is needed to interchange between the different state measurements.

422 leakage After the qubit is initialized in the desired state, and before it is shelved, leakage of 422 nm laser light ruins state initialization. Off resonance laser light used for cooling, and resonant laser light used for detection both have linear polarization and hence can excite either of the Zeeman split levels. As the excited state decays, it might decay to either of the two qubit

states. Therefore, a qubit initialized in either of the levels will decay into an equal statistical mixture of the two states after a sufficiently long time. Leakage of the two beams will hence have an equal effect on the lifetimes of the two qubit states. Leakage of the optical pumping beam will only shorten the lifetime of the $|\downarrow\rangle$ state, since it can't excite population from the $|\uparrow\rangle$ state.

Lifetime of the qubit levels is measured by initializing the qubit in the desired state, waiting for time t_{idle} and then performing shelving. If the ion was initialized in the $|\uparrow\rangle$ state, and remained there, it will be shelved with high probability and appear dark. For $t_{idle} \ll \tau_{|\uparrow\rangle}$, the fraction of experiments in which the ion will be bright is $\frac{t_{idle}}{\tau_{|\uparrow\rangle}}$, up to the error due to imperfect shelving. Similarly, if the ion was initialized in the $|\downarrow\rangle$ state, and remained there, it won't be shelved and will appear bright. The fraction of experiments in which the ion will be dark is $\frac{t_{idle}}{\tau_{|\downarrow\rangle}}$. Finite lifetimes were measured for the two qubit levels at first, but after placing an ND filter on the off resonant beam no decay was observed for neither of the states.

8.3.2 Shelving errors

HO levels distribution As discussed in section 3.3.4 and observed in section 7.2 the thermal distribution of harmonic levels occupied by the ion limits the efficiency of the shelving to $\simeq 99\%$. For the 2^{nd} shelving pulse, we need to take into account the change in level occupation distribution due to the first pulse. During the first pulse, lower n states are shelved with higher efficiency, and we are thus left mostly with higher n's in the $S_{1/2}$ level. Applying another, identical, shelving pulse brings only $\simeq 94\%$ of the remaining population to the $D_{5/2}$ level. Thus, the error in a double shelving sequence is $6 \cdot 10^{-4}$.

Frequency drifts As discussed in section 6.2, the $674\,nm$ laser frequency drifts due to thermal drifts of the ULE cavity. Assuming typical drifts of the cavity temperature of $0.01°C$ in an hour, the drift of the laser is $\delta \simeq 2-3kHz$ in $\simeq 2-3min$. To avoid larger drifts, the resonance frequency of the shelving transition is scanned every few minutes and the frequency of the AOM is corrected accordingly. The decrease in shelving efficiency due to a few kHz drift of the laser, given a Rabi frequency of $\Omega \simeq 50kHz$, is $1 - \frac{\Omega^2}{\Omega^2+\delta^2} \simeq 5 \cdot 10^{-3}$.

Intensity noise Intensity noise of the $674\,nm$ light leads to fluctuations in the Rabi frequency, and therefore affects shelving efficiency. There are a few sources for intensity noise in the system. First, fiber phase noise translated to AM noise when passing through a polarizing beam splitter (PBS) on the way to the ion. This noise is reduced using intensity noise eater as described in section 6.4. Next, beam pointing of the laser beam on the ion. And finally, decrease in the intensity of laser carrier frequency on the expense of energy outside the carrier, if laser frequency noise PSD is increased (e.g. if the laser gets close to a mode-hop). The cumulative effect of all these noise

sources can be estimated by measuring fluctuations in the duration of a π pulse over the course of the experiment. π time was measured every $\simeq 2-3min$ during the experiment (several hours) and fluctuations of $\Delta t_\pi \simeq 0.2\mu s$ were obtained. Note that these fluctuations are comparable to the time resolution of the FPGA, which is limited to $\epsilon_t = \frac{1}{4}\mu s$. Therefore, the contribution of intensity noise, and pulse duration quantization noise is estimated to be $1 - sin^2\left(\frac{\pi}{2}\frac{t_\pi+\epsilon_t}{t_\pi}\right) \simeq 2\cdot 10^{-3}$, for a π time of $t_\pi \simeq 10\mu s$.

Off resonance excitation The frequency of the $S_{1/2,+1/2} \rightarrow D_{5/2,+3/2}$ transition used to shelve the $|\uparrow\rangle$ qubit state, is detuned by $\delta \simeq 4\,MHz$ from the $S_{1/2,-1/2} \rightarrow D_{5/2,+1/2}$ transition. Therefore, if the qubit is initialized in the $|\downarrow\rangle$ state, a maximal population inversion of $\frac{\Omega^2}{\Omega^2+\delta^2} \simeq 0.5\cdot 10^{-4}$ can occur, given Rabi frequency of $\Omega_{S_{1/2,-1/2}\rightarrow D_{5/2,+1/2}} \simeq 33kHz$. Similarly, the frequency of the $S_{1/2,+1/2} \rightarrow D_{5/2,-1/2}$ transition has the same detuning δ from the $S_{1/2,-1/2} \rightarrow D_{5/2,-3/2}$ transition. However, due to the higher Rabi frequency $\Omega_{S_{1/2,-1/2}\rightarrow D_{5/2,-3/2}} \simeq 50kHz$ the maximal population inversion is higher, $\frac{\Omega^2}{\Omega^2+\delta^2} \simeq 1.5\cdot 10^{-4}$. Hence, for double shelving this can contribute an error of up to $2\cdot 10^{-4}$.

Another contribution to off-resonance excitation is due to the residual energy outside the carrier (servo bumps). Although the servo bumps are only $\sim 1\,MHz$ away from the carrier we cannot rule out their contribution $4\,MHz$ away on the $S_{1,2,-1,2} \rightarrow D_{5/2}$ transition. However, at this point we do not have a quantitative estimate of this error.

8.3.3 $D_{5/2}$ lifetime

1033 leakage Leakage of the $1033\,nm$ laser, pumps out population from the $D_{5/2}$ level during the shelving and detection stages. This effectively shortens the lifetime of the level and increases the error due to decay of the ion during the detection. However, this decrease in lifetime can be directly measured with the following experimental sequence: The ion is shelved to $D_{5/2}$ level and fluorescence detection is performed. If the shelving was successful (the ion appears dark) detection is performed again after some time t_{idle}. The expected fraction of experiments in which the ion will appear bright after the second detection is $\frac{t_{idle}}{\tau_{D_{5/2}}}$ for $t_{idle} \ll \tau_{D_{5/2}}$. If leakage is present, the fraction will be higher corresponding to shorter lifetime. An ND filter is placed on the beam branch of the $1033nm$ laser that leads to the ion, to decrease the power of the laser and thus decrease the leakage, until the fraction of experiments in which the ion appeared bright corresponds to the expected value of the lifetime $\tau_{D_{5/2}} = 390\,ms$. To compensate for this decrease in power the repump time at the end of every sequence needs to be prolonged to $1\,ms$.

Error source		$\epsilon_{\|\uparrow\rangle}$
Optical pumping		$\simeq 10^{-3}$
422 leakage		-
HO levels distribution	$1 \cdot 10^{-2}$, $6 \cdot 10^{-2}$	$1.1 \cdot 10^{-3}$
Frequency drifts	$5 \cdot 10^{-3}$	
Intensity noise	$2 \cdot 10^{-3}$	
1033 Leakage		-

(a)

Error source	$\epsilon_{\|\downarrow\rangle}$
Optical pumping	$\simeq 10^{-3}$
RF π pulse	$1 \cdot 10^{-4}$
422 leakage	-
Coherent off resonant excitation	$2 \cdot 10^{-4}$
Incoherent off resonant excitation	*unknown*
1033 Leakage	-

(b)

Table 1: Detection fidelity error budget for the sum of initialization and shelving errors for (a) $|\uparrow\rangle$ qubit state and (b) $|\downarrow\rangle$ qubit state.

8.3.4 Summary

All error sources considered above and their contributions to the error are summarized in table 1. For the dark state, the estimated sum of initialization and shelving errors is somewhat larger than the value obtained from the fit to the measured data - $1.2 \cdot 10^{-3}$. For the bright state, it is somewhat smaller than the value from the fit - $1.6 \cdot 10^{-3}$. It is important to keep in mind that most of the error budget presented here consists of quite rough estimations, meant to give an order of magnitude evaluation for the errors.

9 Summary

In this work we demonstrate the narrowing of the linewidth of an external cavity diode laser at $674\,nm$ to $1\,kHz$ and the stabilization of its frequency by locking it to a high finesse ULE glass cavity. Using this laser we implemented high fidelity state detection of a qubit encoded in the Zeeman splitting of the ground state of a single $^{88}Sr^{+}$ ion.

The limitations on the best effort readout fidelity of 99.81% were analyzed. Our estimates for the contribution of imperfect state initialization to the measured error is $\sim 0.1\%$. Another contribution, of $\sim 0.06\%$, is due to imperfect shelving of one of the qubit states to a metastable level of the ion prior to the state-selective fluorescence detection. The remaining part, $\sim 0.03\%$, results from limited state discrimination efficiency due to the finite lifetime of the metastable level. This error can be reduced to $\sim 0.02\%$ if information on photon arrival times is used. This fraction of the error is intrinsic to the state detection scheme and cannot be decreased further.

The high readout fidelity reached is compatible with recent estimates of the fault-tolerance required error threshold and can be used in the future to implement effective quantum error correction algorithms. In addition it can be used to reach high accuracy and efficiency in implementation of tools like quantum state tomography, and the study of basic quantum processes.

A Appendix

A.1 $S_{1/2} \rightarrow D_{5/2}$ Rabi frequency

Following James [5], the Rabi frequency can be expressed in terms of the reduced matrix element $\langle 5S_{1/2}||r^2C^{(2)}||4D_{5/2}\rangle$ and the Wigner 3-j symbols

$$\Omega_0 = \left| \frac{eE_0\omega_0}{2\hbar c} \langle 5S_{1/2}||r^2C^{(2)}||4D_{5/2}\rangle \sum_{q=-2}^{2} \begin{pmatrix} 1/2 & 2 & 5/2 \\ -m & q & m' \end{pmatrix} c_{ij}^{(q)} \epsilon_i n_j \right|.$$

Here ϵ_i, n_j are the vector components of the polarization, and propagation direction of the beam respectively. $c_{ij}^{(q)}$ are 2^{nd} order tensors given explicitly in [5]. For the direction of the wave vector, $\vec{k}$, used in the experiment (parallel to the quantization axis), the geometrical factor $c_{ij}^{(q)}\epsilon_i n_j$ is non-zero only for $q = \pm 1$, thus allowing only$\Delta m_J = \pm 1$ transitions.

For $q = \pm 1$, $c_{ij}^{(q)}\epsilon_i n_j = \frac{1}{\sqrt{6}}$ and is independent of the polarization of the beam.

The relevant Wigner symbols are

$$\begin{pmatrix} 1/2 & 2 & 5/2 \\ -1/2 & -1 & 3/2 \end{pmatrix} = -\sqrt{\frac{2}{15}} \qquad \begin{pmatrix} 1/2 & 2 & 5/2 \\ -1/2 & 1 & -1/2 \end{pmatrix} = -\sqrt{\frac{1}{15}}$$
$$\begin{pmatrix} 1/2 & 2 & 5/2 \\ 1/2 & -1 & 1/2 \end{pmatrix} = \sqrt{\frac{1}{15}} \qquad \begin{pmatrix} 1/2 & 2 & 5/2 \\ 1/2 & 1 & -3/2 \end{pmatrix} = \sqrt{\frac{2}{15}},$$

leading to the following relations between the Rabi frequencies

$$\begin{aligned} \Omega_0\left(S_{1/2,+1/2} \rightarrow D_{5/2,-1/2}\right) &= \frac{1}{\sqrt{2}}\Omega_0\left(S_{1/2,+1/2} \rightarrow D_{5/2,+3/2}\right) \\ \Omega_0\left(S_{1/2,-1/2} \rightarrow D_{5/2,-3/2}\right) &= \Omega_0\left(S_{1/2,+1/2} \rightarrow D_{5/2,+3/2}\right) \\ \Omega_0\left(S_{1/2,-1/2} \rightarrow D_{5/2,+1/2}\right) &= \Omega_0\left(S_{1/2,+1/2} \rightarrow D_{5/2,-1/2}\right). \end{aligned}$$

The reduced matrix element is related to the decay rate of the excited state, A, by

$$A = \frac{c\alpha k^5}{15\left(2j'+1\right)} \left|\langle 5S_{1/2}||r^2C^{(2)}||4D_{5/2}\rangle\right|^2 \Rightarrow$$
$$\left|\langle S_{1/2}||r^2C^{(2)}||D_{5/2}\rangle\right| = \sqrt{\frac{15\left(2j'+1\right)}{c\alpha k^5}A} = \sqrt{\frac{15\cdot 6}{c\alpha k^5}A},$$

where $j' = 5/2$ was substituted in the last step.

Using the well known relation between the intensity of the laser and the electric field of the laser, $I = \frac{c\epsilon_0 n}{2} E^2$, as well as the relation between the intensity and the power, $I = \frac{P}{\frac{1}{2}\pi w^2}$ (here$w$ is the waste of the Gaussian beam on the ion) we obtain

$$E = \sqrt{\frac{2}{c\epsilon_0 n} I} = \frac{2}{\sqrt{\pi}} \sqrt{\frac{P}{c\epsilon_0 n w^2}}.$$

Calculating the Rabi frequency in detail for the $S_{1/2,+1/2} \rightarrow D_{5/2,+3/2}$ transition

$$\Omega_0 \left(S_{1/2,1/2} \rightarrow D_{5/2,3/2} \right) = \left| \frac{eE_0\omega_0}{2\hbar c} \sqrt{\frac{15 \cdot 6}{c\alpha k^5} A} \sqrt{\frac{2}{15}} \frac{1}{\sqrt{6}} \right| = \frac{eE_0}{2\hbar} \sqrt{\frac{2}{c\alpha k^3} A} =$$
$$\frac{e}{\sqrt{\pi}\hbar} \sqrt{\frac{P}{c\epsilon_0 n w^2}} \sqrt{\frac{2}{c\frac{e^2}{\hbar c 4\pi\epsilon_0} k^3} A} = \sqrt{\frac{8PA}{\hbar c n w^2 k^3}} = (2\pi)\, 53kHz,$$

where the decay rate of $D_{5/2}$ level, $A = \frac{1}{\tau_{D_{5/2}}} = 2.56\frac{1}{s}$, was used and laser power of $P = 120\mu W$ with beam waste of $w = 30\mu m$ on the ion were assumed.

A.2 Dark state probability density function

The probability density function for the number of detected photons in the dark state, given a finite lifetime of the $D_{5/2}$ level given in Eq. 16 and replicated here is

$$p_d(n) = \left(1 - \frac{t_{det}}{\tau}\right) Poiss\left(n,\, R_d t_{det}\right) +$$
$$\int_0^{t_{det}} dt' \frac{1}{\tau} \sum_{k=0}^{n} Poiss\left(k,\, R_d t'\right) Poiss\left(n-k,\, R_b\left(t_{det} - t'\right)\right). \quad (33)$$

The sum appearing in the second term can be written explicitly using the definition of the Poisson distribution,

$$\sum_{k=0}^{n} Poiss\left(k,\, R_d t'\right) Poiss\left(n-k,\, R_b\left(t_{det}-t'\right)\right) =$$

$$\sum_{k=0}^{n} \frac{\left(R_d t'\right)^k e^{-R_d t'}}{k!} \cdot \frac{\left(R_b\left(t_{det}-t'\right)\right)^{n-k} e^{-R_b\left(t_{det}-t'\right)}}{(n-k)!} =$$

$$\frac{e^{-\left[R_b\left(t_{det}-t'\right)+R_d t'\right]}}{n!} \sum_{k=0}^{n} \frac{n!}{k!\,(n-k)!} \left(R_d t'\right)^k \left(R_b\left(t_{det}-t'\right)\right)^{n-k} =$$

$$\frac{e^{-\left[R_b\left(t_{det}-t'\right)+R_d t'\right]}}{n!} \left[R_b\left(t_{det}-t'\right)+R_d t'\right]^n = Poiss\left(n,\, \bar{n}\right). \quad (34)$$

Thus Eq. 17 is obtained, where the weighed mean number of photons is defined as

$$\bar{n} = R_b\left(t_{det}-t'\right) + R_d t' = \frac{\bar{n}_b}{t_{det}}\left(t_{det}-t'\right) + \frac{\bar{n}_d}{t_{det}} t' = \bar{n}_b\left(1-\frac{t'}{t_{det}}\right) + \bar{n}_d \frac{t'}{t_{det}}. \quad (35)$$

The second term in Eq. 33 can now be written as

$$\int_0^{t_{det}} dt' \frac{1}{\tau} \sum_{k=0}^{n} Poiss\left(k,\, R_d t'\right) Poiss\left(n-k,\, R_b\left(t_{det}-t'\right)\right) \quad = \quad \int_0^{t_{det}} dt' \frac{1}{\tau} Poiss\left(n,\, \bar{n}\right). \quad (36)$$

Performing a change of variables from t' to $\bar{n}$,

$$d\bar{n} = -\frac{dt'}{t_{det}}\left(\bar{n}_b - \bar{n}_d\right) \Rightarrow dt' = -\frac{t_{det}}{\left(\bar{n}_b - \bar{n}_d\right)} d\bar{n} \quad (37)$$

and adjusting the limits of integration accordingly, $t'=0 \rightarrow \bar{n}=\bar{n}_b$, $t'=t_{det} \rightarrow \bar{n}=\bar{n}_d$, the integral can be evaluated with the use of the incomplete gamma function $\Gamma\left(x,a\right) = \frac{1}{\Gamma(a)} \int_0^x e^{-t} t^{a-1} dt$,

$$\int_0^{t_{det}} dt' \frac{1}{\tau} Poiss\left(n,\, \bar{n}\right) = \frac{t_{det}}{\tau} \frac{1}{\left(\bar{n}_b - \bar{n}_d\right)} \int_{\bar{n}_d}^{\bar{n}_b} \frac{1}{n!} \bar{n}^n e^{-\bar{n}} d\bar{n} = \frac{t_{det}}{\tau} \frac{\Gamma\left(\bar{n}_b\, n+1\right) - \Gamma\left(\bar{n}_d,\, n+1\right)}{\left(\bar{n}_b - \bar{n}_d\right)}, \quad (38)$$

and Eq. 18 obtained.

References

[1] E.D. Black. An introduction to Pound–Drever–Hall laser frequency stabilization. *American Journal of Physics*, 69:79, 2001.

[2] F. Bondu and O. Debieu. Accurate measurement of Fabry-Perot cavity parameters via optical transfer function.

[3] D.P. DiVincenzo. The physical implementation of quantum computation. *Scalable quantum computers: Paving the way to realization*, page 1, 2001.

[4] L.K. Grover. Quantum mechanics helps in searching for a needle in a haystack. *Physical Review Letters*, 79(2):325–328, 1997.

[5] DFV James. Quantum dynamics of cold trapped ions with application to quantum computation. *Applied Physics B: Lasers and Optics*, 66(2):181–190, 1998.

[6] E. Knill. Quantum computing with realistically noisy devices. *Nature*, 434(7029):39–44, 2005.

[7] D. Leibfried, R. Blatt, C. Monroe, and D. Wineland. Quantum dynamics of single trapped ions. *Rev. Mod. Phys.*, 75(1):281–324, Mar 2003.

[8] V. Letchumanan, MA Wilson, P. Gill, and AG Sinclair. Lifetime measurement of the metastable $4d\,^2D_{5/2}$ state in $^{88}Sr^+$ using a single trapped ion. *Physical Review A*, 72(1):12509, 2005.

[9] AD Ludlow, X. Huang, M. Notcutt, T. Zanon-Willette, SM Foreman, MM Boyd, S. Blatt, and J. Ye. Compact, thermal-noise-limited optical cavity for diode laser stabilization at 1×10^{-15} . *Optics Letters*, 32(6):641–643, 2007.

[10] AH Myerson, DJ Szwer, SC Webster, DTC Allcock, MJ Curtis, G. Imreh, JA Sherman, DN Stacey, AM Steane, and DM Lucas. High-fidelity readout of trapped-ion qubits. *Physical Review Letters*, 100(20):200502, 2008.

[11] M. A. Nielsen and I. L Chuang. *Quantum Computation and Quantum Information*. Cambridge University Press, 2000.

[12] W. Paul. Electromagnetic traps for charged and neutral particles. *Reviews of Modern Physics*, 62(3):531–540, 1990.

[13] K. Petermann. *Laser diode modulation and noise*. Springer, 1991.

[14] C. Roos. *Controlling the quantum state of trapped ions*. PhD thesis, Ph. D. thesis, Universität Innsbruck, 2000.

[15] A.L. Schawlow and C.H. Townes. Infrared and optical masers. *Physical Review*, 112(6):1940–1949, 1958.

[16] P.W. Shor. Polynomial-time algorithms for prime factorization and discrete logarithms on a quantum computer. *SIAM Review*, 41(2):303–332, 1999.

[17] A. E. Siegman. *Lasers*. University Science Books, 1986.

[18] GM Stephan, TT Tam, S. Blin, P. Besnard, and M. Têtu. Laser line shape and spectral density of frequency noise. *Physical Review A*, 71(4):43809, 2005.

[19] D. J. Wineland, C. Monroe, W. M. Itano, D. Leibfried, B. E. King, and D. M. Meekhof. Experimental issues in coherent quantum-state manipulation of trapped atomic ions. *J.RES.NATL.INST.STAND.TECH.*, 103:259, 1998.

[20] A. Yariv. *Quantum Electronics*.